Published online: July 25, 2016

Article

SOURCE DATA | TRANSPARENT PROCESS

THE EMBO JOURNAL

Tryptophan-rich basic protein (WRB) mediates insertion of the tail-anchored protein otoferlin and is required for hair cell exocytosis and hearing

Christian Vogl[1,2,†], Iliana Panou[1,2,3,†], Gulnara Yamanbaeva[2,4,†], Carolin Wichmann[2,5,†], Sara J Mangosing[6,†], Fabio Vilardi[7,†], Artur A Indzhykulian[8,†], Tina Pangršič[2,9,†], Rosamaria Santarelli[10,11], Montserrat Rodriguez-Ballesteros[12], Thomas Weber[1], Sangyong Jung[1,13], Elena Cardenas[6], Xudong Wu[8], Sonja M Wojcik[14], Kelvin Y Kwan[15], Ignacio del Castillo[12,16], Blanche Schwappach[7], Nicola Strenzke[2,4], David P Corey[8,*], Shuh-Yow Lin[6,**] & Tobias Moser[1,2,13,17,***]

Abstract

The transmembrane recognition complex (TRC40) pathway mediates the insertion of tail-anchored (TA) proteins into membranes. Here, we demonstrate that otoferlin, a TA protein essential for hair cell exocytosis, is inserted into the endoplasmic reticulum (ER) via the TRC40 pathway. We mutated the TRC40 receptor tryptophan-rich basic protein (Wrb) in hair cells of zebrafish and mice and studied the impact of defective TA protein insertion. Wrb disruption reduced otoferlin levels in hair cells and impaired hearing, which could be restored in zebrafish by transgenic Wrb rescue and otoferlin overexpression. Wrb-deficient mouse inner hair cells (IHCs) displayed normal numbers of afferent synapses, Ca^{2+} channels, and membrane-proximal vesicles, but contained fewer ribbon-associated vesicles. Patch-clamp of IHCs revealed impaired synaptic vesicle replenishment. *In vivo* recordings from postsynaptic spiral ganglion neurons showed a use-dependent reduction in sound-evoked spiking, corroborating the notion of impaired IHC vesicle replenishment. A human mutation affecting the transmembrane domain of otoferlin impaired its ER targeting and caused an auditory synaptopathy. We conclude that the TRC40 pathway is critical for hearing and propose that otoferlin is an essential substrate of this pathway in hair cells.

Keywords deafness; endoplasmic reticulum; protein targeting; synapse; tail-anchored protein

Subject Categories Neuroscience

DOI 10.15252/embj.201593565 | Received 30 November 2015 | Revised 29 May 2016 | Accepted 10 June 2016 | Published online 25 July 2016

The EMBO Journal (2016) 35: 2536–2552

See also: **KB Avraham** (December 2016)

Introduction

TA proteins are integral membrane proteins that comprise a single transmembrane domain at the distal C-terminus and a N-terminus

1 Institute for Auditory Neuroscience and InnerEarLab, University Medical Center Göttingen, Göttingen, Germany
2 Collaborative Research Center 889, University of Göttingen, Göttingen, Germany
3 Göttingen Graduate School for Neurosciences, Biophysics and Molecular Biosciences, University of Göttingen, Göttingen, Germany
4 Auditory Systems Physiology Group and InnerEarLab, Department of Otolaryngology, University of Göttingen Medical Center, Göttingen, Germany
5 Molecular Architecture of Synapses Group, Institute for Auditory Neuroscience and InnerEarLab, University Medical Center Göttingen, Göttingen, Germany
6 Otolaryngology Division, Department of Surgery, School of Medicine, University of California San Diego, La Jolla, CA, USA
7 Institute of Molecular Biology, University Medical Center Göttingen, Göttingen, Germany
8 Howard Hughes Medical Institute and Department of Neurobiology, Harvard Medical School, Boston, MA, USA
9 Synaptic Physiology of Mammalian Vestibular Hair Cells Junior Research Group, Institute for Auditory Neuroscience and InnerEarLab, University Medical Center Göttingen, Göttingen, Germany
10 Department of Neurosciences, University of Padova, Padova, Italy
11 Audiology and Phoniatrics Service, Treviso Regional Hospital, Treviso, Italy
12 Servicio de Genetica, Hospital Universitario Ramon y Cajal, IRYCIS, Madrid, Spain
13 Synaptic Nanophysiology Group, Max Planck Institute for Biophysical Chemistry, Göttingen, Germany
14 Department of Molecular Neurobiology, Max-Planck-Institute for Experimental Medicine, Göttingen, Germany
15 W. M. Keck Center for Collaborative Neuroscience, Nelson Lab-D250, Rutgers University, Piscataway, NJ, USA
16 Centro de Investigacion Biomedica en Red de Enfermedades Raras (CIBERER), Madrid, Spain
17 Center for Nanoscale Microscopy and Molecular Physiology of the Brain, University Medical Center Göttingen, Göttingen, Germany
*Corresponding author. Tel: +1 617 432 2506; E-mail: david_corey@hms.harvard.edu
**Corresponding author. Tel: +1 858 822 3297; E-mail: shuh-yow@ucsd.edu
***Corresponding author. Tel: +49 551 3922803; E-mail: tmoser@gwdg.de
†These authors contributed equally to this work

that is oriented toward the cytoplasm. This group includes numerous essential proteins such as cytochrome b5, Bcl-2 (B-cell lymphoma 2), the soluble N-ethylmaleimide-sensitive-factor attachment receptors (SNAREs) synaptobrevin and syntaxin, as well as ferlins (Kalbfleisch *et al*, 2007). TA proteins reside in various intracellular compartments like the outer membranes of mitochondria, nuclei, secretory organelles, or plasma membranes. TA proteins of the secretory pathway are post-translationally inserted into the ER. This process is mediated by the highly homologous "guided entry of TA proteins" (GET)/TRC40/Asna1 pathway that has been studied extensively in yeast and mammalian cell lines in culture (Simpson *et al*, 2010; Denic *et al*, 2013; Yamamoto & Sakisaka, 2015) (Fig 1A). However, the role of the TRC40 pathway in the context of native cells, tissues, or organisms has yet to be investigated. Unlike the co-translational membrane insertion of most other proteins, the membrane insertion of TA proteins is uncoupled from translation and involves (i) recognition by TRC40 (Stefanovic & Hegde, 2007; Favaloro *et al*, 2008), (ii) targeting to the TRC40 receptors WRB (Vilardi *et al*, 2011) and calcium-modulating cyclophilin ligand (CAML) (Yamamoto & Sakisaka, 2012) on the ER membrane and finally, (iii) ATP-dependent unbinding from TRC40 and insertion into the target membrane [as shown for Get3, the yeast homologue of TRC40 (Bozkurt *et al*, 2009; Mateja *et al*, 2009; Suloway *et al*, 2009)] (Fig 1A).

Based on evidence collected from yeast (Schuldiner *et al*, 2005, 2008), disruption of the TRC40 pathway for TA protein insertion is likely to have pleiotropic detrimental effects given the relevance of the various TA proteins for cellular functions. The general importance of the TRC40 pathway is highlighted by embryonic lethality upon constitutive genetic ablation of *Trc40* in mice (Mukhopadhyay *et al*, 2006). Moreover, recent studies in mice and zebrafish have pointed toward a fundamental role of the TRC40 pathway in sensory function. For instance, genetic deletion of *Caml* (Bryda *et al*, 2012) in sensory hair cells (HCs) led to HC loss and deafness in mice. While the underlying mechanisms were not further elucidated in this study, a role of Caml in hair cell development/function via its interaction with the tip-link protein cadherin 23 was favored over a requirement for TA protein insertion. Moreover, a retroviral insertional mutagenesis screen has identified a zebrafish *wrb* mutant (*pinball wizard*, *pwi*; Amsterdam *et al*, 2004), with impairments of visual and auditory function (Gross *et al*, 2005; Lin *et al*, 2016).

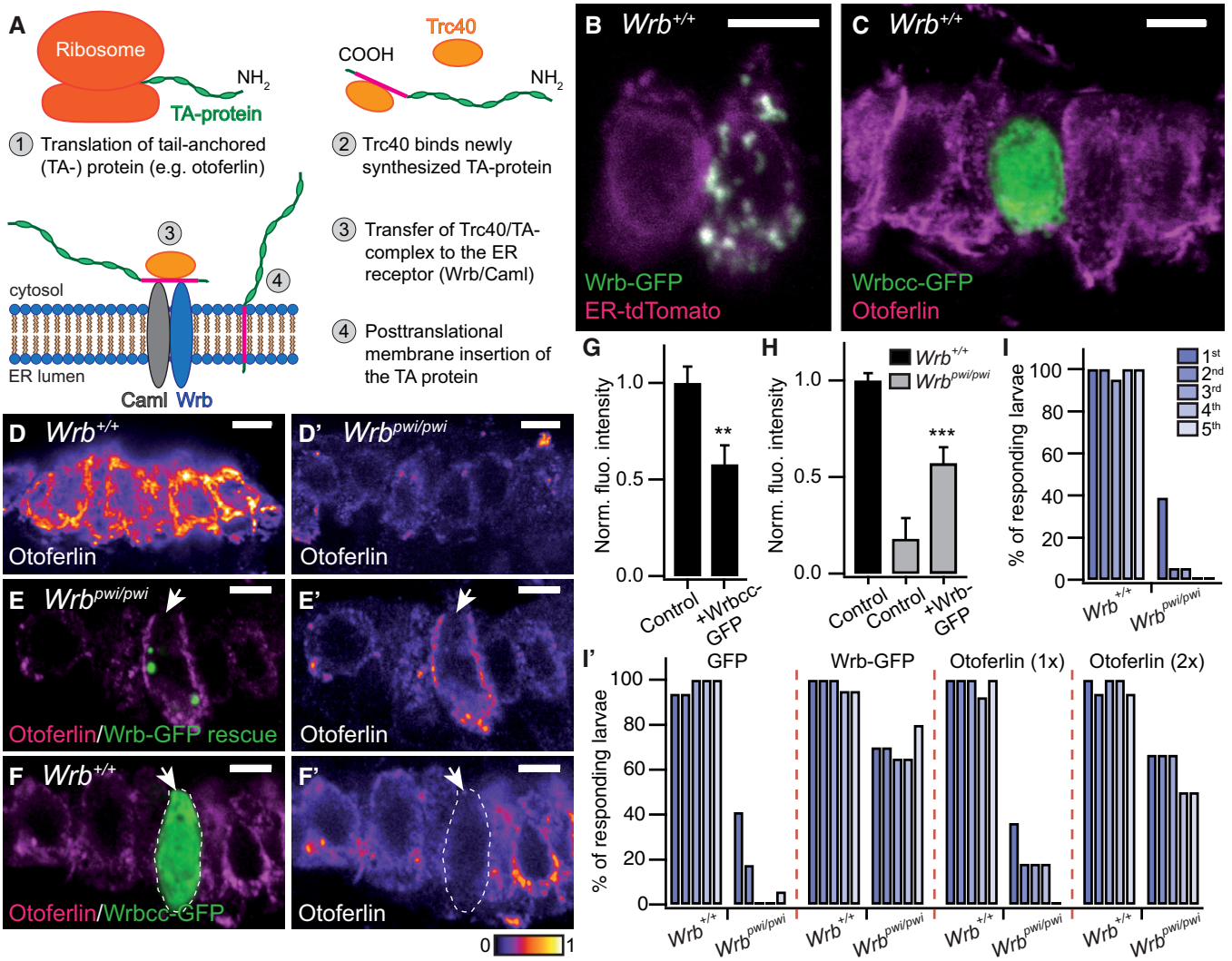

Figure 1.

Here, we studied the role of the TRC40 pathway in sensory HCs of zebrafish and mice. We focused our analysis on the effects of Wrb disruption on otoferlin, one of several TA proteins expressed in HCs. Otoferlin is involved in synaptic vesicle fusion and replenishment (Roux *et al*, 2006; Dulon *et al*, 2009; Pangrsic *et al*, 2010; Vogl *et al*, 2015), and its disruption causes deafness in human and mice (Yasunaga *et al*, 1999; Roux *et al*, 2006; Varga *et al*, 2006; Marlin *et al*, 2010). Combining genetic, biochemical, cell biological, and physiological approaches, we demonstrate a critical role of the TRC40 pathway in the biogenesis of otoferlin, HC exocytosis, and hearing.

Results

The TRC40 pathway mediates the ER-insertion of otoferlin and is critical for normal otoferlin abundance in HCs

In order to explore the expression and functional organization of the TRC40 pathway (Fig 1A) in HCs, we expressed Wrb with a C-terminal GFP-tag in zebrafish. As expected for an ER-resident protein, we found spot-like Wrb-GFP signal mostly co-localized with a recombinant fluorescent ER marker (ER-tdTomato; Fig 1B) in saccular HCs. In contrast, a truncated version of GFP-tagged Wrb, containing the coiled-coil domain, but lacking the transmembrane domains (Wrbcc; Vilardi *et al*, 2011), was diffusely distributed throughout the HC cytoplasm (Fig 1C). We assume that the spot-like Wrb distribution in zebrafish HCs (Fig 1B and E) reflects a distorted ER morphology due to overexpression of the full-length Wrb.

The zebrafish mutant *pwi*, with disrupted *wrb* (Amsterdam *et al*, 2004), lacks the acoustic startle reflex as a consequence of impaired HC function (Lin *et al*, 2016). In *pwi* fish, we found a strong reduction in otoferlin levels in HCs of the inner ear (Fig 1D and D′) and lateral line neuromasts (Fig EV1). Here, transgenic expression of GFP-tagged wild-type Wrb restored otoferlin expression (Fig 1E and H), and with capped Wrb-GFP mRNA injection, startle reflex was partially rescued (Fig 1I′). This indicates that the TRC40 pathway is required for both HC membrane insertion of otoferlin and hearing in zebrafish. Consistent with the requirement of the TRC40 pathway for sufficient otoferlin biogenesis, overexpression of Wrbcc in wild-type zebrafish reduced HC otoferlin levels (Fig 1F, F′ and G), likely reflecting a dominant negative effect due to competition with wild-type Wrb (Vilardi *et al*, 2011). In order to test whether the impaired auditory function of *pwi* fish relates to otoferlin deficiency, we sought to override the disrupted ER targeting by overexpression (Schuldiner *et al*, 2008) of otoferlin. Indeed, we could partially restore the startle response by otoferlin overexpression in a dose-dependent manner (Fig 1I′), suggesting that disrupted ER targeting of otoferlin contributes to the impairment of auditory function in *pwi* fish.

Next, we turned to an *in vitro* post-translational membrane insertion assay to verify the hypothesis that the TRC40 pathway mediates ER targeting of otoferlin. Here, a recombinant opsin-tagged otoferlin, comprising the C-terminal transmembrane segment and parts of the N-terminus, was co-expressed and co-purified in complex with wild-type or mutant TRC40 (Fig 2). Purified TRC40 and otoferlin were incubated with rough microsomes (RM) derived from pancreatic ER. Membrane insertion of otoferlin was detected as a shift in molecular mass due to glycosylation of the C-terminal opsin tag of otoferlin (OTOFop). The latter can only take place upon membrane insertion, as shown previously for the TA protein RAMP4 (Favaloro *et al*, 2010). Stimulated membrane insertion was observed for otoferlin complexed with wild-type, but not with mutant TRC40 (Fig 2A and B).

Figure 1. The TRC40 pathway is present in HCs and is critical for normal otoferlin abundance and hearing in zebrafish.

A Simplified schematic representation of the post-translational membrane insertion pathway of tail-anchored (TA) proteins.

B The ER marker ER-tdTomato (magenta) is co-localized with ectopically expressed Wrb-EGFP (green) in saccular HCs of 5-dpf zebrafish larvae ("control" refers to either wild-type or *+/pwi* fish that were picked in a phenotypic screen and did not exert any abnormal behavioral phenotype). While the left HC solely expressed ER-tdTomato, the neighboring HC expressed both ER-tdTomato and Wrb-GFP. Colocalization between both proteins occurs in areas exhibiting white pixels. Scale bar: 5 μm.

C Projection of confocal sections of control inner ear HCs immunolabeled for otoferlin (magenta) and expressing an EGFP-tagged truncated Wrb fragment containing only the cytosolic coiled-coil domains (Wrbcc-EGFP, green). Wrbcc-EGFP distribution was diffuse and found throughout the HC. Scale bar: 5 μm.

D, D′ Projection of confocal sections of inner ear HCs of 5-dpf control (D) and Wrb-deficient *pwi* mutant fish ($wrb^{pwi/pwi}$; D′), showing strongly reduced otoferlin immunofluorescence in the mutant HCs. The color lookup table used represents higher pixel intensities with warmer colors. Scale bar: 5 μm.

E, E′ A representative transgenically rescued *pwi* mutant HC (white arrow), expressing Wrb-GFP, exhibits a strongly increased otoferlin signal (magenta) in direct comparison with the neighboring non-rescued mutant HCs. (E′) Same image as in (E) but intensity-coded for otoferlin fluorescence. Scale bar: 5 μm.

F, F′ A representative control HC expressing Wrbcc-EGFP (white arrow), immunolabeled for otoferlin (magenta). The Wrbcc-EGFP-expressing HC shows significantly less otoferlin (F′), suggesting a dominant negative effect of Wrbcc in otoferlin biogenesis. The transfected HC is encircled with a dashed line. Scale bar: 5 μm.

G Quantification of otoferlin downregulation by Wrbcc-EGFP overexpression shown in (F). Otoferlin immunofluorescence intensity of Wrbcc-EGFP transfected inner ear HCs (n = 22, from three 5-dpf control larva) showed a significant decrease in fluorescence intensity of ~43% compared to the adjacent Wrbcc-EGFP-negative wild-type HCs (n = 22, from the same larva). Fluorescent intensity values were normalized with the average value of Wrbcc-EGFP-negative HCs. Data are represented as means ± SEM. $^{**}P < 0.01$.

H Quantification of otoferlin immunohistochemistry data shown in (E) from hair cells of control (n = 88 HCs from three 5-dpf larva), $wrb^{pwi/pwi}$ (n = 80 HCs from 3 sibling larva) normalized against the mean intensity value of the control group and Wrb-GFP transfected $wrb^{pwi/pwi}$ zebrafish inner ears. Mutant HCs showed ~82% reduction in otoferlin fluorescence intensity when compared with control HCs imaged under the same conditions. Otoferlin fluorescent intensity of Wrb-EGFP-transfected mutant HCs (n = 24, from three 5-dpf larva) showed significant increases compared to adjacent Wrb-EGFP-negative mutant HCs (n = 24 from the same larva). Fluorescent intensity values were normalized with the average value of wild-type HCs. Data are represented as means ± SEM. $^{***}P < 0.001$

I, I′ Acoustic startle reflex measurements of (I) live, intact, 5-dpf control zebrafish larva (n = 20) where almost 100% of the larva responded repeatedly to five successive acoustic stimuli at 3-s intervals. In $wrb^{pwi/pwi}$ animals (n = 18), only 39% of larva responded to the first stimulus, thereafter, the number of responding larva decreased rapidly to less than 6%. (I′) Acoustic startle reflexes of 5-dpf zebrafish larva after injection with either EGFP capped mRNA (control, n = 16, or $wrb^{pwi/pwi}$ n = 17), Wrb-EGFP capped mRNA (control, n = 20, or $wrb^{pwi/pwi}$ n = 20), or two different concentrations of otoferlin mRNA (1×: control, n = 13; $wrb^{pwi/pwi}$ n = 11; 2×: control, n = 16; $wrb^{pwi/pwi}$ n = 6). In contrast to EGFP mRNA injection, Wrb-EGFP as well as otoferlin mRNAs could partially rescue the acoustic startle reflex in the mutants, while not displaying detrimental effects on overall zebrafish morphology and development. Please note the dose-dependent effect of otoferlin mRNA injection. Similar results as in 1× EGFP mRNA were also obtained from injection of 2× EGFP mRNA as control (data not shown). Measurements from two (2× otoferlin) or three (all other) different experiments were compiled in the graph.

Published online: July 25, 2016

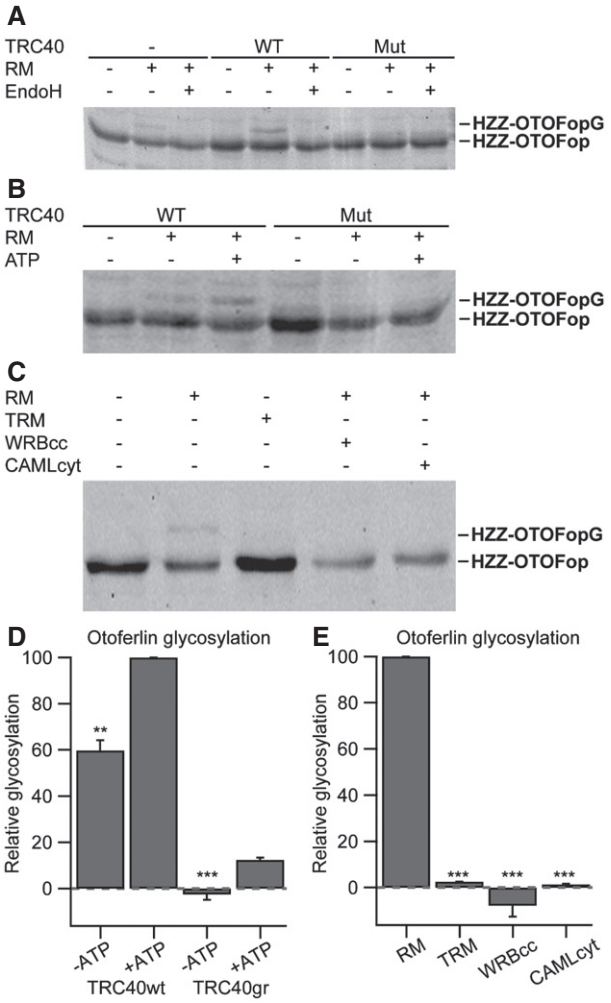

Figure 2. The TRC40 pathway mediates the insertion of otoferlin into mammalian ER-derived microsomes.

A HZZ-OTOFop, carrying a C-terminal glycosylation site (opsin tag), was purified alone or in complex with wild-type or an ATPase-deficient mutant version of TRC40 and incubated in the absence or presence of ER-derived rough microsomes (RM). Membrane integration (glycosylation) was monitored by SDS–PAGE and immunoblot using an anti-opsin antibody. Where indicated, EndoH was used to remove *N*-linked oligosaccharides.

B HZZ-OTOFop in complex with wild-type or mutant TRC40 was incubated with RM in the presence or absence of ATP and membrane insertion was monitored by opsin-specific immunoblot.

C HZZ-OTOFop in complex with wild-type TRC40 was incubated in the presence of RM or trypsin-treated rough microsomes (TRM), and in the presence of WRBcc or CAMLcyt. Membrane insertion was monitored by opsin-specific immunoblot.

D Quantification of relative protein glycosylation shown in (B) (n = 3). Data are represented as means ± SEM. TRC40gr, mutated version of TRC40; $^{**}P < 0.01$; $^{***}P < 0.001$ (Student's two-sample t-test).

E Quantification of relative protein glycosylation of the data shown in (C) (n = 3). Data are represented as means ± SEM. $^{***}P < 0.001$ (Student's two-sample t-test).

Source data are available online for this figure.

Otoferlin insertion was further promoted by ATP (Fig 2B and D), albeit less than previously found for RAMP4, and inhibited by incubation with either the competing coiled-coil domains of WRBcc or CAML cytosolic domain (CAMLcyt) (Fig 2C and E). We further validated these findings by *in vitro* ER integration of otoferlin in combination with immunodepletion of TRC40 in the reticulocyte lysate and found that otoferlin insertion appears to exclusively require TRC40, but not the alternative HSC70 pathway (Rabu *et al*, 2008), which was tested in parallel (Appendix Fig S1A–C). This, however, does not rule out the likely possibility that the HSC70 pathway mediates the residual ER targeting of otoferlin in *wrb*-deficient hair cells (Fig 1). In general, the efficiency of otoferlin insertion in this *in vitro* assay was relatively low in comparison with other TA proteins, which might relate to the truncation of otoferlin. In summary, our data indicate that the TRC40 pathway is the key mediator of otoferlin insertion into ER-derived microsomes that occurs in an ATP-dependent manner, and is indispensable to establish normal abundance of otoferlin in HCs.

Targeted disruption of the *Wrb* gene in mouse sensory IHCs causes a synaptic hearing impairment

For an in-depth analysis of the role of the TRC40 pathway in HCs, we generated conditional *Wrb* knockout mice by flanking exons two to four by *loxP* sites via homologous recombination ($Wrb^{fl/fl}$, Fig EV2A). $Wrb^{fl/fl}$ mice were viable and could be bred in homozygosity. In order to achieve IHC-specific Cre recombination, we crossed $Wrb^{fl/fl}$ mice with mice expressing Cre-recombinase under control of the vesicular glutamate transporter (Vglut3) promoter. Vglut3 expression is restricted to hair cells (Obholzer *et al*, 2008; Ruel *et al*, 2008; Seal *et al*, 2008) and to some classes of neurons (reviewed in El Mestikawy *et al*, 2011). We used two independent *Vglut3-Cre* mouse lines (Fig EV2B): (i) A transgenic line in which Cre-recombinase (but no additional Vglut3) was expressed under the control of the transgenic *Vglut3* promoter (Jung *et al*, 2015; here and below referred to as Cre^{A}) and (ii) a knock-in mouse, in which *Cre* was inserted into the *Vglut3* locus following an internal ribosomal entry site [(Lou *et al*, 2013), here and below referred to as Cre^{B}]. Genotyping was performed by PCR on tail DNA for all transgenes (Fig EV2C). When probing Cre activity with reporter mice (Nakamura *et al*, 2006; Madisen *et al*, 2010), recombination within the cochlea was confined to IHCs with only very few OHCs showing reporter gene expression in both mouse lines (Appendix Fig S2A–C). In addition, recombination was evident in some capillaries and few glial cells (Appendix Fig S2A and B). $Wrb^{fl/fl}$:Cre^{A} mice grew slower than $Wrb^{+/+}$:Cre^{A} littermates (Appendix Fig S2D) and progressively experienced tonic–clonic seizures that, in some cases, lasted for several minutes (Video EV1). We suspect that this neurological phenotype resulted from *Wrb* disruption in Vglut3-expressing inhibitory CNS neurons.

$Wrb^{fl/fl}$:Cre^{A} mice showed strongly impaired auditory brainstem responses (ABRs, Fig 3). We found a progressive reduction in the amplitude of ABR wave 1 (spiral ganglion compound action potential, Fig 3A–A″) and an elevation of ABR thresholds across all frequencies tested (Fig 3B–B″). In order to obtain an early estimate of auditory function, we also analyzed mice during the third postnatal week, right after the onset of hearing, when auditory sensitivity is not yet fully mature (Fig 3A and B). At all ages tested (groups I: P14–17; II: P21–26; III: > P29), we encountered $Wrb^{fl/fl}$:Cre^{A} mice lacking ABRs even with the strongest stimuli that our speaker could deliver (at a given frequency or for the click,

Published online: July 25, 2016
The EMBO Journal

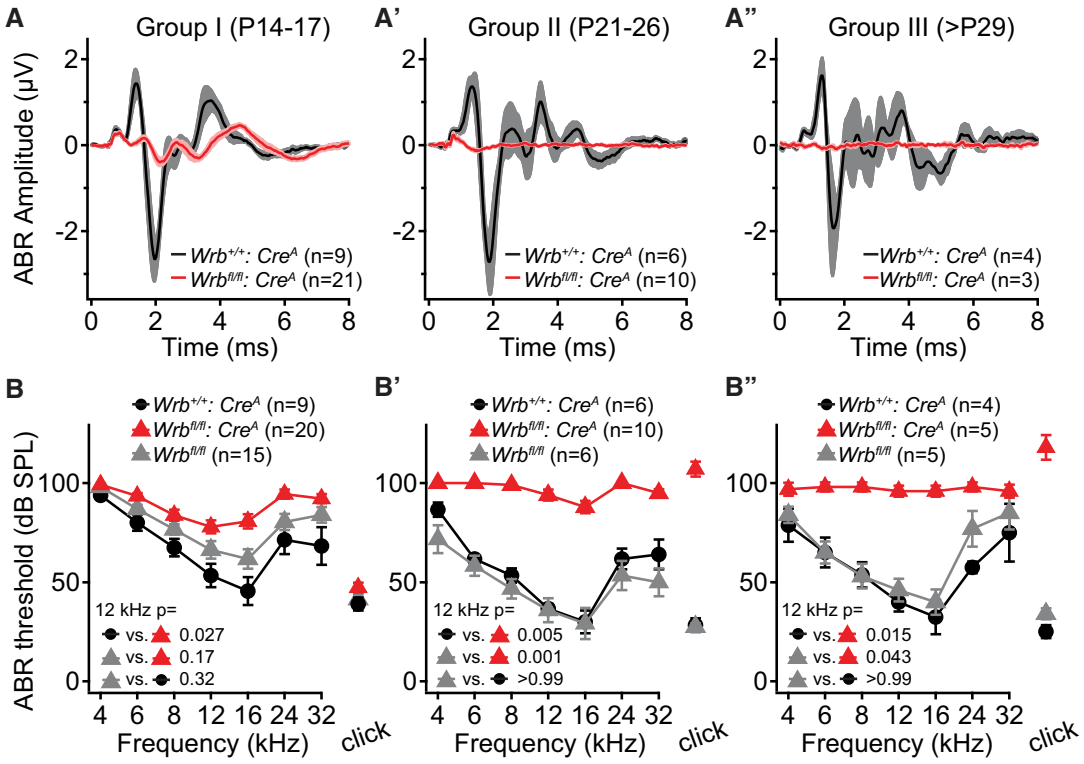

Figure 3. Wrb disruption in IHCs causes a progressive hearing impairment in mice.

A–A″ Grand averages of auditory brainstem responses (ABRs) from $Wrb^{fl/fl}$:Cre^{A} (red traces, SEM pink) and $Wrb^{+/+}$:Cre^{A} (black traces, SEM gray) mice. ABRs were recorded for three separate age groups (A–A″, as indicated in the graph) using click stimulation at 80 dB (peak equivalent) and 20 Hz stimulation rate. There was an age-progressive reduction in ABR amplitude in $Wrb^{fl/fl}$:Cre^{A} mice.

B–B″ ABRs from $Wrb^{fl/fl}$:Cre^{A} mice showed a progressive threshold increase, and $Wrb^{+/+}$:Cre^{A} mice and $Wrb^{fl/fl}$ mice lacking Cre-recombinase had normal thresholds. Statistical comparison of the threshold at 12 kHz was done by Kruskal–Wallis test, and *P*-values are from *post hoc* Dunn's multiple comparison test. Measurements in which no ABR was observed at the maximal available tone burst level (90 dB) or click level (120 dB) scored as 100 dB threshold. Data are represented as means ± SEM.

Appendix Table S1). These were scored as 100 dB thresholds, therefore providing a conservative estimate of the mean hearing impairment. Similarly, a profound hearing impairment was confirmed for $Wrb^{fl/fl}$:Cre^{B} mice (9–16 weeks old, Fig EV3G). DPOAEs were present with normal input–output functions in $Wrb^{fl/fl}$:Cre^{A} mice across all frequencies tested (Fig EV3C–E), confirming intact OHC function, which was expected since only very few OHCs showed Cre activity (Appendix Fig S2A–C).

To investigate whether impaired mechanoelectrical transduction of IHCs contributed to the hearing impairment of $Wrb^{fl/fl}$:*Cre* mice, we studied hair bundle morphology and function. Fluorophore-coupled phalloidin stainings in $Wrb^{+/+}$:Cre^{A} and $Wrb^{fl/fl}$:Cre^{A} mice (P14 IHCs; Fig EV4F) as well as scanning electron microscopy (SEM) of P6 and P10 IHCs from $Wrb^{fl/fl}$:Cre^{B} mice (Fig EV4A) revealed normal development and maintenance of IHC hair bundles. We tested mechanoelectrical transduction (MET) in HCs using short application of 2 µM FM1-43, a lipophilic styryl-dye (30 s, Fig EV4B), which efficiently permeates active mechanoelectrical transducer channels (Gale *et al*, 2001; Meyers *et al*, 2003) and generates a robust staining of the intracellular membranes. Weak staining due to endocytosis is possible (Revelo *et al*, 2014), but this pathway was greatly minimized due to the short dye application. We observed comparable FM1-43 staining of hair cells in the organ of Corti and the utricle in P7 $Wrb^{+/fl}$:Cre^{B} and $Wrb^{fl/fl}$:Cre^{B} mice (Fig EV4B), suggesting preserved MET. To further test IHC transduction, we performed whole-cell patch-clamp recordings of mechanoelectrical transducer currents upon stereocilia bundle deflection in $Wrb^{+/fl}$:Cre^{B} and $Wrb^{fl/fl}$:Cre^{B} mice, which showed currents of comparable amplitude and adaptation (Fig EV4C–F, also showing OHC data). Together, impaired ABR despite intact MET and cochlear amplification points toward perturbed sound encoding at the IHC synapse, a phenotype designated as auditory synaptopathy (Moser & Starr, 2016).

Wrb-deficient IHCs exhibit reduced otoferlin levels

Our evidence for Wrb-dependent otoferlin membrane insertion and its requirement for hearing in zebrafish (Figs 1 and 2) together with the implication of otoferlin disruption in auditory synaptopathy (Rodríguez-Ballesteros *et al*, 2003; Varga *et al*, 2003; Roux *et al*, 2006), led us to study the effects of Wrb disruption on the abundance and localization of otoferlin in mouse IHCs (Fig 4). We found a strong reduction in otoferlin immunofluorescence intensity levels in IHCs of $Wrb^{fl/fl}$:Cre^{A} mice. By the beginning of the third postnatal

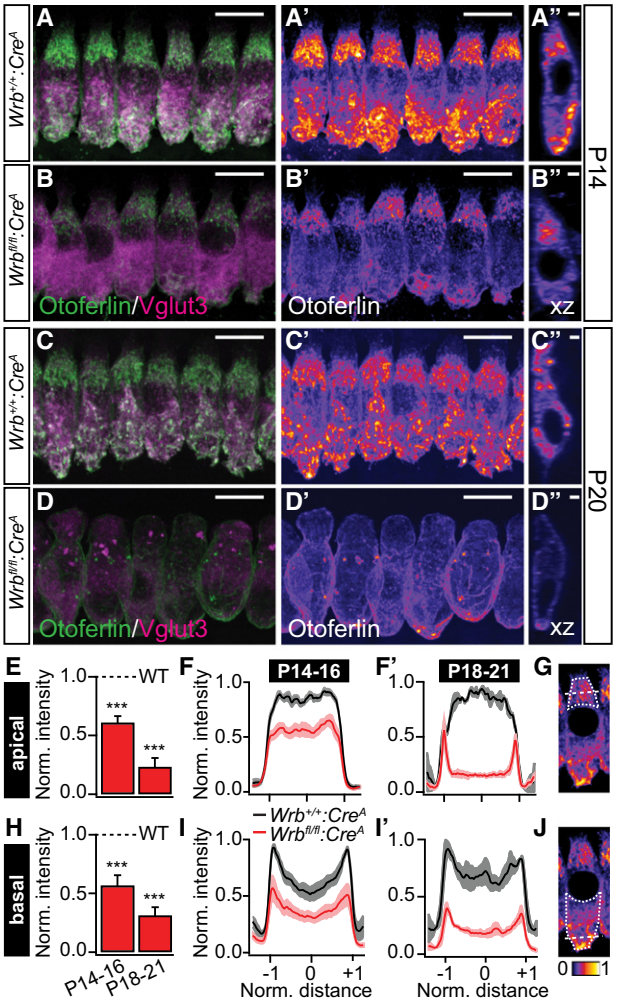

Figure 4. Wrb disruption in mouse IHCs greatly reduced otoferlin levels.

A–D″ Representative maximum projections of confocal sections of (A–B″) P14 and (C–D″) P20 $Wrb^{+/+}$:Cre^A and $Wrb^{fl/fl}$:Cre^A apical turn organs of Corti following immunolabeling against otoferlin (green) and Vglut3 (magenta) processed and imaged under identical conditions. Panels (A′, B′, C′, and D′) show individual otoferlin stainings with an intensity-coded lookup table. Panels (A″, B″, C″, and D″) present single *xz* projections at a central point through a representative IHC to illustrate otoferlin subcellular distribution. Scale bars in (A, A′, B, B′, C, C′, D, D′) represent 10 μm, in (A″, B″, C″, D″) 2 μm. Note the dramatic reduction in otoferlin fluorescence and the alteration in its distribution as well as a change in cell shape and position of nuclei (for detailed analysis of cell shape and nuclei position, please refer to Fig EV5).

E–G Semiquantitative analysis of otoferlin immunofluorescence in the apical parts of IHCs from $Wrb^{fl/fl}$:Cre^A mice using averaged regions of interests in cell's maximal projections (outlined with a dotted line in G for a single representative IHC) normalized to the maximum values observed in the respective control IHCs. Averaged supranuclear coronal line profiles, as illustrated with a dashed line in (G), are shown for (F) P14–16 and (F′) P18-21 IHCs. ***$P < 0.001$ versus $Wrb^{+/+}$:Cre^A.

H–J Semiquantitative analysis of otoferlin immunofluorescence in the basal parts of IHCs from $Wrb^{fl/fl}$:Cre^A mice using averaged regions of interests in cell's maximal projections (outlined with a dotted line in J for a single representative IHC) normalized to the maximum values observed in the respective control IHCs. Averaged supranuclear coronal line profiles, as illustrated with a dashed line in (J), are shown for (I) P14–16 and (I′) P18–21 IHCs. ***$P < 0.001$ versus $Wrb^{+/+}$:Cre^A.

Data information: All data are represented as grand averages of individual cell means ± SEM normalized to their respective $Wrb^{+/+}$:Cre^A control.

week (P14-16), otoferlin levels were decreased to ~61% and 57% of that in $Wrb^{+/+}$:Cre^A mice in the apical and basal parts of Wrb-deficient IHCs, respectively (Fig 4A, B and E–H; $n = 99$ and 83 IHCs from five $Wrb^{fl/fl}$:Cre^A and four $Wrb^{+/+}$:Cre^A animals, respectively). Otoferlin levels further decreased to 23% (apex) and 31% (base) of wild-type levels (Fig 4C–H) in IHCs of P18–21 animals ($n = 62$ and 64 IHCs from five $Wrb^{fl/fl}$:Cre^A and five $Wrb^{+/+}$:Cre^A animals, respectively), which we attribute to impaired biogenesis of otoferlin. In parallel, we found an increased abundance of the lysosomal marker LAMP1 in $Wrb^{fl/fl}$:Cre^A IHCs (Appendix Fig S3C), which might reflect increased degradation of non-inserted TA proteins such as otoferlin. In contrast, the abundance and localization of the IHC synaptic vesicle marker Vglut3 appeared unchanged (Fig 4A–D). Wrb-deficient IHCs further exhibited altered overall cell shape and nuclear position (Fig EV5). While we cannot exclude that this resulted from perturbed membrane insertion of TA proteins involved in the organization of the cytoskeleton (e.g. nesprin 4, Horn *et al*, 2013), we note that IHC shape was similarly altered in mice carrying a point mutation in the *Otof* gene [i.e. *pachanga* mice; (Pangrsic *et al*, 2010)]. *Pachanga* mice also contain reduced levels of otoferlin, suggesting that the observed changes in cell shape could be related to abundance and/or function of otoferlin (Appendix Table S2).

Wrb disruption in IHCs alters the structure and function of hair cell ribbon synapses

Next, we studied the number, structure and function of IHC ribbon synapses, the most likely site of failure, given the IHC-specific genetic manipulation and auditory system phenotype. Synapse formation and gross synaptic morphology were unaltered, as assessed by immunohistochemical analysis of presynaptic ribbons (RIBEYE/CtBP2) and postsynaptic AMPA receptor clusters (GluA2/3) during the third postnatal week (Appendix Table S3). Specifically, unlike synapses in *Bsn* mutant mice (Khimich *et al*, 2005), almost all synapses were occupied by synaptic ribbons. Moreover, in contrast to the findings in *Otof* knockout mice (Roux *et al*, 2006), the number of synapses in $Wrb^{fl/fl}$:Cre^A animals was comparable to wild type (Appendix Table S3).

Transmission electron microscopy confirmed proper anchorage of the ribbons to the presynaptic density at the ultrastructural level (Fig 5A and B). However, quantitative analysis of random ultrathin sections revealed a reduced number of ribbon-associated vesicles on the distal half of the $Wrb^{fl/fl}$:Cre^A IHC ribbons (Fig 5C–F). In contrast, the number of membrane-proximal synaptic vesicles at the active zone, thought to represent the morphological correlate of the readily releasable pool (RRP) of vesicles, remained unchanged. In addition, we found that subplasmalemmal cisternae near synaptic sites were often decorated with electron-dense particles, most likely representing ribosomes (Fig 5B, B′ and C). Quantification of random ultrathin sections revealed that ~36% $Wrb^{fl/fl}$:Cre^A synapses showed such structures within a distance of 200 nm or less from the presynaptic density ($n = 41$ sections; see also tomographic reconstruction in Appendix Fig S3D and D′), whereas this was observed at only ~4% of $Wrb^{+/+}$:Cre^A synapses ($n = 25$ sections). This might

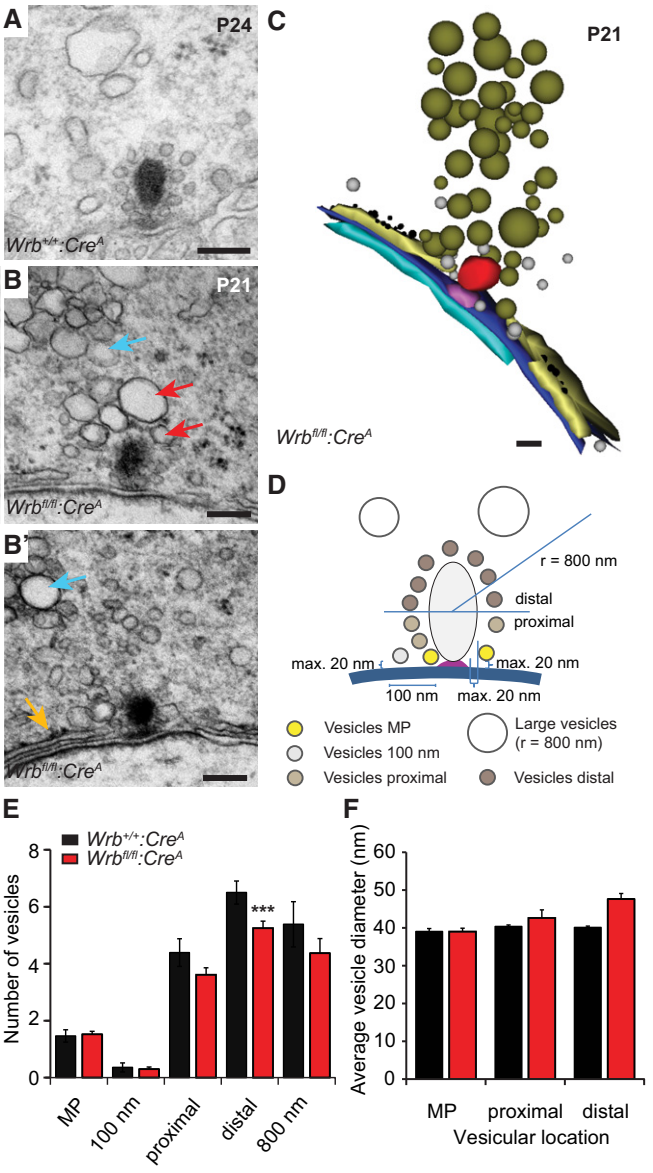

Figure 5. Fewer ribbon-associated synaptic vesicles, but perisynaptic accumulation of cisternal organelles and rough ER in Wrb-deficient IHCs.

A Representative electron micrograph of a $Wrb^{+/+}$:Cre^{A} IHC ribbon synapse. Scale bar: 120 nm.

B, B′ In $Wrb^{fl/fl}$:Cre^{A} (depicted are two consecutive ultrathin sections) IHCs, accumulations of large partially amorphous vesicles were observed close to ribbon synapses (red arrows), but also further away in the cytoplasm (cyan arrows). Moreover, cisternal structures resembling (r)ER are found unusually close to the ribbon (orange arrow in B′). Scale bar: 120 nm.

C 3D serial reconstruction of the ribbon synapse depicted in (B, B′, using "Reconstruct" software). Scale bar: 100 nm.

D Schematic illustration of the quantitative analysis performed on random ultrathin sections, results shown in (E) and (F).

E Quantification in random ultrathin sections ($Wrb^{+/+}$:Cre^{A} n = 28, from two animals; $Wrb^{fl/fl}$:Cre^{A} n = 44, from three animals) of the numbers of membrane-proximal "MP" vesicles (in close proximity to membrane and ribbon); vesicles within a 100 nm range along the active zone membrane; vesicles at the lower "proximal" and the upper "distal" half of the ribbon as well as vesicles > 70 nm ("large vesicles") in a radius of 800 nm around the ribbon. The vesicle number was significantly reduced in $Wrb^{fl/fl}$:Cre^{A} IHCs at the distal part of the ribbon, but not at the presynaptic membrane or proximal ribbon part. Data are represented as means ± SEM. Student's two-sample t-test, $^{***}P < 0.001$.

F Average vesicle diameters of the membrane-proximal vesicles and the vesicles at both halves of the ribbon. The mean vesicle diameter is unchanged in $Wrb^{fl/fl}$:Cre^{A} IHCs. Data are represented as means ± SEM.

reflect a compensatory up-regulation of perisynaptic ER, triggered by impaired TA protein insertion. We further found a perisynaptic accumulation of large pleomorphic membranous organelles that were more prominent in $Wrb^{fl/fl}$:Cre^{A} animals [28% of $Wrb^{+/+}$:Cre^{A} synapses (n = 25 sections) versus $Wrb^{fl/fl}$:Cre^{A} ~36% (n = 41 sections); Fig 5B, B′ and C]. Interestingly, in $Wrb^{fl/fl}$:Cre^{A}, these organelles appeared to accumulate within IHC basal regions also away from the active zones (Appendix Fig S3). They might either represent accumulations of endosome-like vacuoles formed by bulk endocytosis, which persist due to impaired vesicle reformation, or possibly lysosomes (Appendix Fig S3C and C'). Other aspects of hair cell morphology, such as the Golgi apparatus, cytoplasmic ER, and cuticular plate, did not show obvious changes (Appendix Fig S3A and B′).

Next, in order to study presynaptic function, we performed perforated patch-clamp recordings from P14 to P17 IHCs. We found that Ca^{2+} currents of $Wrb^{fl/fl}$:Cre^{A} IHCs exhibited normal voltage dependence and amplitudes (Fig 6A). This finding is consistent with the normal synapse number and overall morphology of IHC active zones in Wrb-deficient IHCs at 2–3 weeks of age (Appendix Table S3 and Fig 5). Exocytosis evoked by this Ca^{2+} influx, monitored as increments in membrane capacitance (ΔC_m), was normal in Wrb-deficient IHCs for stimuli < 20 ms, but was reduced for longer stimuli (Fig 6B–E). Vesicle fusion and Ca^{2+} influx–exocytosis coupling appeared unaltered, given that ΔC_m was normal for stimuli shorter than 20 ms, which primarily recruit the RRP (Moser & Beutner, 2000; Fig 6D). As exocytosis elicited by longer stimuli is thought to primarily report replenishment and subsequent fusion of vesicles (Moser & Beutner, 2000; Spassova *et al*, 2004; Cho *et al*, 2011; Goutman, 2012; Pangršič *et al*, 2015) and fusion was intact, we interpret the reduction in such sustained exocytosis to reflect impaired vesicle replenishment. A similar, but more pronounced reduction in vesicle resupply was observed in IHCs from deaf *pachanga* otoferlin mutants (Pangrsic *et al*, 2010; replotted for comparison in Fig 6D). The Ca^{2+} efficiency of exocytosis, measured as the $\Delta C_m/Q_{Ca^{2+}}$ ratio, was lower in *Wrb* mutants compared to control for stimuli of 20 ms and longer (Fig 6E). Finally, Wrb-deficient IHCs were smaller in surface area than controls (basal membrane capacitance: 8.2 ± 0.5 versus 9.5 ± 0.3 pF, P = 0.002, Wilcoxon rank test) and therein comparable to otoferlin knockout ($Otof^{-/-}$) IHCs (8.3 ± 0.3 pF; Pangrsic *et al*, 2010; see also our analysis of cell size and shape in Fig EV5 and Appendix Table S2).

Wrb deletion in IHCs disrupts sound encoding

We next turned to *in vivo* extracellular recordings from individual spiral ganglion neurons (SGNs). As each SGN is driven by a single presynaptic IHC active zone, this technique permits analysis of synaptic function at the single synapse level, using physiological stimulation *in vivo*. All SGNs from $Wrb^{fl/fl}$:Cre^{A} mice had

Published online: July 25, 2016

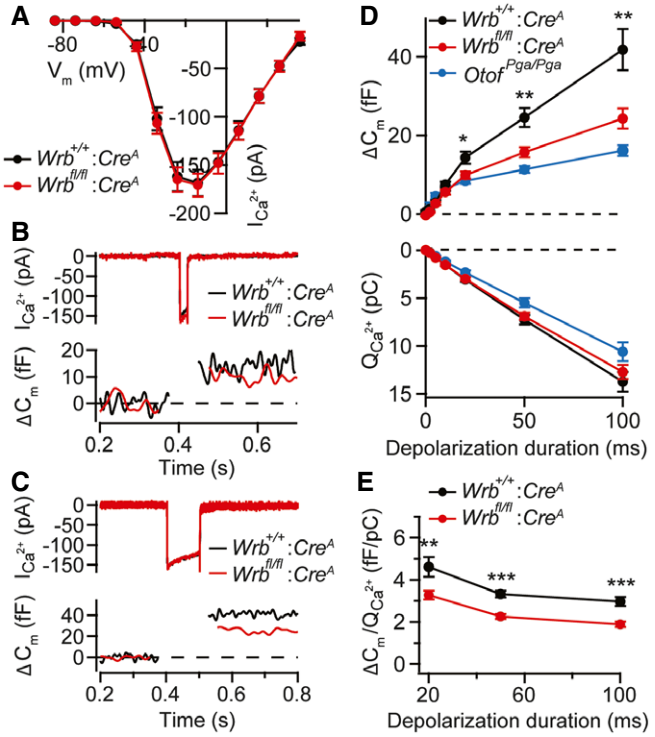

Figure 6. Impaired sustained exocytosis in Wrb-deficient IHCs.

A Ca^{2+} current–voltage relationship of P14–P17 IHCs of $Wrb^{fl/fl}$:Cre^A (n = 17 IHCs) and $Wrb^{+/+}$:Cre^A (n = 15 IHCs) mice in 2 mM extracellular [Ca^{2+}] showed no change in amplitude or voltage dependence of Ca^{2+} currents. Data are represented as means ± SEM.

B Representative Ca^{2+} current (top) and C_m changes (bottom) in $Wrb^{fl/fl}$:Cre^A and $Wrb^{+/+}$:Cre^A IHCs in response to 20-ms step depolarizations to −14 mV (the potential eliciting the maximum Ca^{2+} current).

C Representative Ca^{2+} current (top) and C_m changes (bottom, finite impulse response filtered) in $Wrb^{fl/fl}$:Cre^A and $Wrb^{+/+}$:Cre^A IHCs in response to 100-ms step depolarizations to −14 mV.

D Exocytic ΔC_m (top) and corresponding Ca^{2+} current integrals, Q_{Ca} (bottom) for various depolarization durations. Data are grand averages of the cells' means. Exocytic ΔC_m was reduced in the knockout from 20 ms onwards, indicating reduced sustained exocytosis. Data from $Otof^{Pga/Pga}$ animals were replotted for direct comparison from Pangrsic *et al* (2010). Data represent means ± SEM; *$P < 0.05$; **$P < 0.01$.

E $\Delta C_m/Q_{Ca2+}$ ratio indicates a lower efficacy of Ca^{2+} influx in driving exocytosis in $Wrb^{fl/fl}$:Cre^A IHCs, for stimuli of 20 ms or longer. Data represent means ± SEM; **$P < 0.01$; ***$P < 0.001$.

spontaneous rates lower than 20 Hz, unlike in $Wrb^{+/+}$:Cre^A, where SGNs with high spontaneous rates are also readily found (Fig 7A). Sound-evoked SGN firing was much better preserved than in *pachanga* otoferlin mutants (Pangrsic *et al*, 2010) and, thus, enabled a detailed analysis of sound encoding which, so far, was lacking for mutants with otoferlin deficiency. Frequency tuning (Fig 7B) and acoustic thresholds (Fig 7C) were not significantly changed in $Wrb^{fl/fl}$:Cre^A SGNs. Peak firing rates at sound onset, spike rate adaptation, and adapted firing rates were studied in response to 50 ms-long tone bursts. In these experiments, we used P16–21 $Wrb^{fl/fl}$:Cre^A mice, for which ABRs had indicated present—albeit impaired—afferent auditory signaling. Tones were played at characteristic frequency and saturating sound pressure levels (30 dB above threshold) for three different stimulus repetition rates (2, 5 and 10 Hz, Fig 7D–D″). The resulting post-stimulus time histograms (Fig 7D–D″) showed a use-dependent reduction in onset and adapted firing rates in SGNs from $Wrb^{fl/fl}$:Cre^A mice (Fig 7E), whereby firing rates decreased when stimulation rates increased (Fig 7F). Nonetheless, the firing was much better preserved than for SGNs of otoferlin-deficient *pachanga* mutants (dotted lines in Fig 7D–D″). Consistent with the rate reduction, the median latency of the first spikes (FSL) in response to stimulus onset was dramatically increased (10.9 ± 1.4 ms in $Wrb^{fl/fl}$:Cre^A, n = 10 versus 4.5 ± 0.2 ms in $Wrb^{+/+}$:Cre^A, n = 29, Fig 7F) and showed enhanced jitter (standard deviation of the FSL: 7.7 ± 1.3 ms in $Wrb^{fl/fl}$:Cre^A, n = 10 versus 1.5 ± 0.3 ms in $Wrb^{+/+}$:Cre^A, n = 29). Together with the reduced peak rate, this reduced synchrony of firing likely explains the strong ABR phenotype in $Wrb^{fl/fl}$:Cre^A mice (see Fig 3).

In order to further test the hypothesis that the replenishment of readily releasable vesicles is impaired at the active zones of Wrb-deficient IHCs, we studied the recovery of onset firing after application of an adapting stimulus (forward masking, Harris & Dallos, 1979). Adaptation is considered to reflect partial depletion of the RRP, while recovery from adaptation likely reflects RRP replenishment (Schroeder & Hall, 1974; Furukawa & Matsuura, 1978; Moser & Beutner, 2000; Spassova *et al*, 2004; Goutman & Glowatzki, 2007; Frank *et al*, 2010; Cho *et al*, 2011). Consistent with a slowed vesicle replenishment at the active zones of $Wrb^{fl/fl}$:Cre^A IHCs, we observed a stronger adaptation, and slower recovery of evoked firing following adaptation (Fig 7G). Together, these results indicate that the reduced vesicle replenishment rate in $Wrb^{fl/fl}$:Cre^A mice lowers the vesicular occupancy of the release sites (i.e. the size of the standing RRP) *in vivo*, resulting in impaired sound encoding. Such a phenotype is not expected for *ex vivo* IHC capacitance measurements. There, IHCs are voltage-clamped to hyperpolarized potentials for 1–2 min between stimulations, which closes all Ca^{2+} channels, thereby prohibiting Ca^{2+}-evoked exocytosis to consume vesicles. This enables vesicle replenishment to refill all release sites, such that the standing RRP is full in $Wrb^{fl/fl}$:Cre^A IHCs despite impaired replenishment.

Deletion of a conserved isoleucine residue in otoferlin's transmembrane domain impairs its integration into the ER

The requirement of Wrb-mediated efficient ER targeting of otoferlin for hearing in zebrafish—as well as the similar IHC exocytosis phenotype of $Wrb^{fl/fl}$:Cre^A mice when compared to the *pachanga* otoferlin missense mutant—suggested that the hearing impairment of $Wrb^{fl/fl}$:Cre^A mice might primarily result from impaired otoferlin biogenesis. In order to further address this hypothesis, we considered mutations in the transmembrane domain (TMD) that might potentially affect post-translational ER targeting of otoferlin as a putative cause of human disease. For the TA protein emerin, several mutations causing Emery–Dreifuss muscular dystrophy have been shown to affect TRC40-dependent targeting (Pfaff *et al*, 2016). Interestingly, we found an in-frame deletion of a conserved isoleucine in the TMD at position 1967 (p.Ile1967del) in a hearing-impaired child of Italian descent (human subject E952-II:1). Sequencing of all exons and exon–intron junctions of the *OTOF* gene of this child revealed two novel variants, c.5401dupG in exon 44 and c.5900_5902delTCA in exon 48, coding for the transmembrane domain, as well as three known polymorphic variants (c.244C > T, c.2829C > T, and

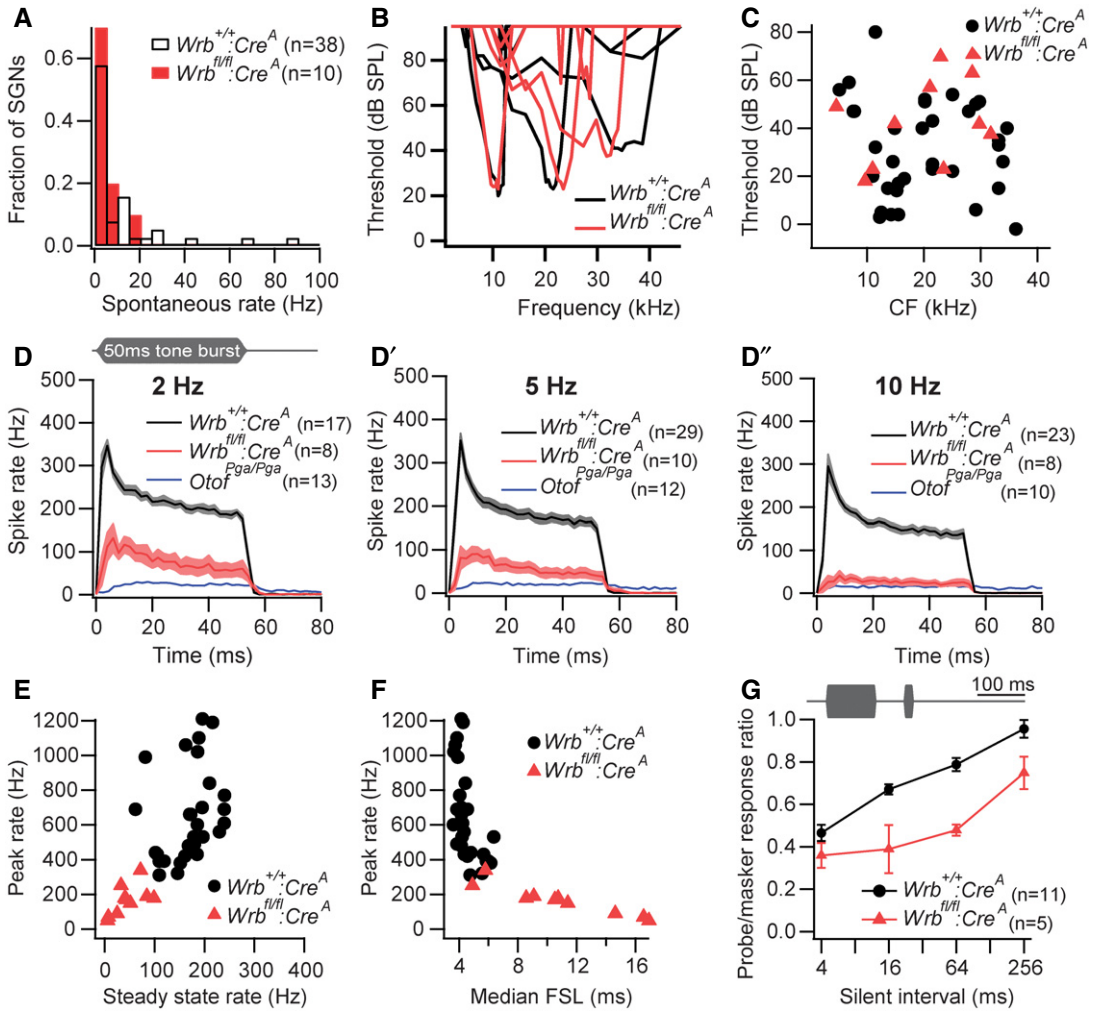

Figure 7. Impaired sound encoding at afferent IHC synapses.

A All SGNs of $Wrb^{fl/fl}$:Cre^{A} mice had spontaneous firing rates (SR) below 20 Hz ($P > 0.05$, Kolmogorov–Smirnov test).

B Representative tuning curves from $Wrb^{fl/fl}$:Cre^{A} and $Wrb^{+/+}$:Cre^{A} SGNs indicating preserved active cochlear amplification despite disruption of Wrb in IHCs.

C Normal thresholds at the characteristic frequency (CF) in $Wrb^{fl/fl}$:Cre^{A} SGNs.

D–D″ Mean poststimulus time histograms (PSTH) ± SEM of $Wrb^{fl/fl}$:Cre^{A} and $Wrb^{+/+}$:Cre^{A} SGNs in response to 50 ms tone bursts presented at CF, 30 dB above threshold at stimulus rates of 2 Hz (D), 5 Hz (D′), or 10 Hz (D″). While the general response pattern was preserved, spike rates were drastically reduced in $Wrb^{fl/fl}$:Cre^{A} SGNs, especially at higher stimulus rates. Data from auditory neurons (SGN and cochlear nucleus) of $Otof^{Pga/Pga}$ animals from Pangrsic *et al* (2010) were replotted for direct comparison.

E Spike rates in response to sound onset (maximum rate in PSTH with 0.5 ms binwidth) and adapted rates (averaged between 35 and 45 ms after stimulus onset) were significantly lower in $Wrb^{fl/fl}$:Cre^{A} SGNs (stimulus rate 5 Hz, $P < 0.001$).

F In line with the reduction in spike rates, first spike latency (FSL) following stimulus onset was greatly increased in $Wrb^{fl/fl}$:Cre^{A} SGNs compared to $Wrb^{+/+}$:Cre^{A} (stimulus rate 5 Hz, $P < 0.001$).

G Illustration of the stimulus paradigm for forward masking experiments: a 100-ms masker tone presented at CF, 30 dB above threshold was followed by a silent interval of variable duration and a 15-ms probe tone (CF, 30 dB above threshold). Bottom: in $Wrb^{fl/fl}$:Cre^{A} SGNs, the response to the first 5 ms of the masker probe tone (shown as a fraction of the response to the first 5 ms of the masker) was strongly reduced, and the half time of recovery (from normalized curves) was increased from 39.2 ± 12.2 ms in $Wrb^{+/+}$:Cre^{A} to 215.7 ± 51.2 ms in $Wrb^{fl/fl}$:Cre^{A} SGNs ($P < 0.001$, Mann–Whitney *U*-test). Data represent means ± SEM.

c.4936C > T), all of which occurred in the heterozygous state (Fig 8A). Additional sequencing of the parental exons 44 and 48 revealed the carrier status and confirmed patient compound heterozygosity for the two novel variants (Fig 8B). Mutation c.5401dupG causes a frameshift that leads to a premature stop codon (p. Ala1801Glyfs*41), and therefore, most likely is inactivating due to subsequent degradation of the transcript by nonsense-mediated decay. Mutation c.5900_5902delTCA results in an in-frame deletion (p.Ile1967del) and was classified as "disease causing" by Mutation Taster (http://www.mutationtaster.org/, score 0.99996). Both mutations were absent from the genomic databases of the NHLBI Exome Sequencing Project (http://evs.gs.washington.edu/EVS/), the Exome Aggregation Consortium (ExAC; http://exac.broadinstitute.org/), and the 1000-Genomes Project (http://browser.1000genomes.org/). We concluded that both of these mutations are pathogenic, whereby the frameshift fully inactivates one

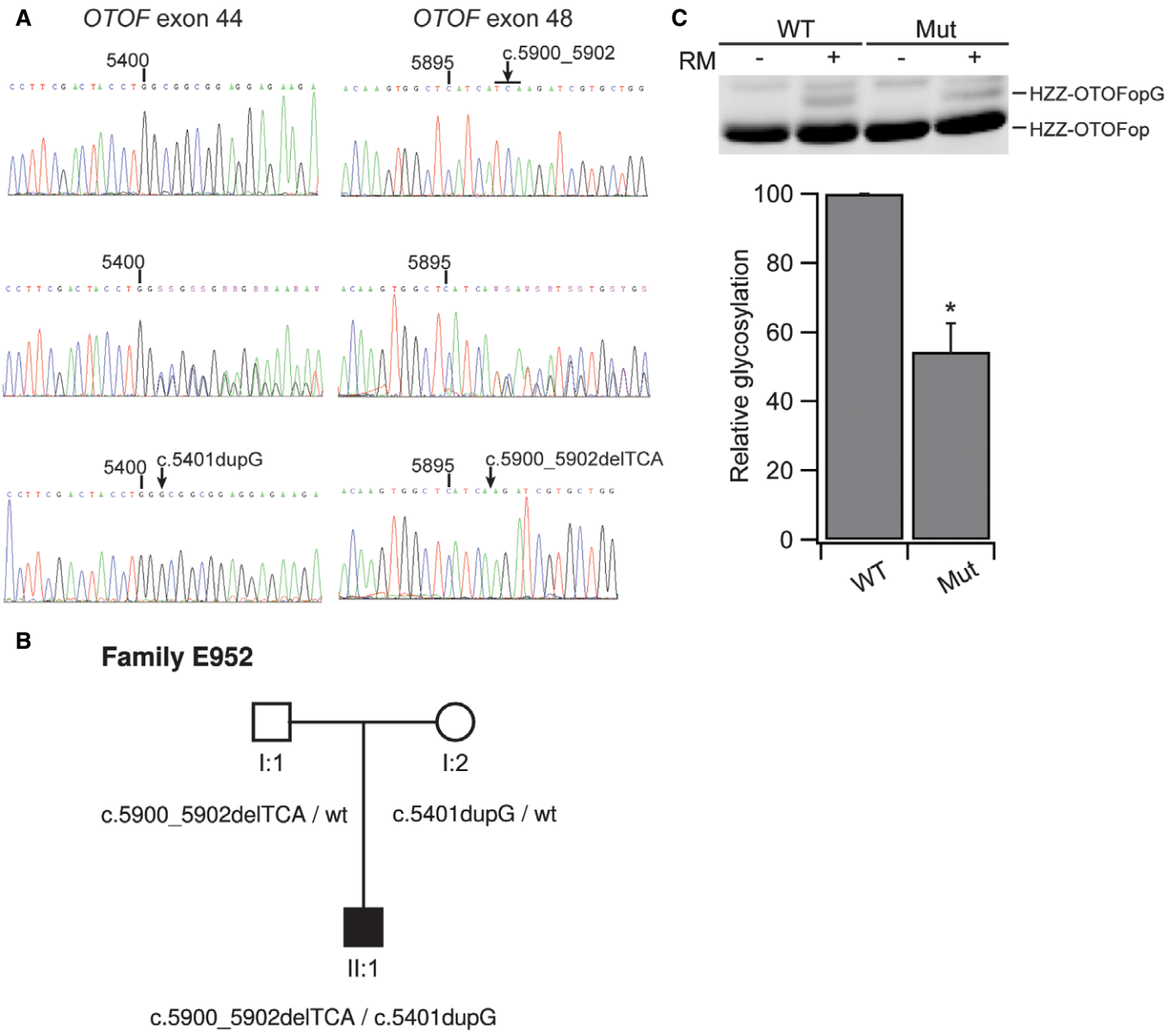

Figure 8. Isoleucine deletion in the transmembrane domain of otoferlin causes impaired ER targeting *in vitro* and hearing impairment in a human patient.

A Electropherograms of the sequences containing the mutations observed in family E952. Position within the *OTOF* cDNA (NM_001287489.1) is indicated above each sequence. For each mutation, the wild-type sequence and the heterozygous sequence are shown. For purposes of clarity, the two alleles carried by subject E952-II:1 were subcloned into a plasmid vector and sequenced in separation. Sequences of the subcloned mutant alleles are shown in the bottom row.

B Pedigree of family E952 showing the segregation of mutations in the *OTOF* gene.

C Apparent decrease in insertion efficiency for the TMD mutant version. While the WT otoferlin glycosylation amounted to 3.84 ± 0.53, the TMD mutant had only 2.13 ± 0.65 (n = 3, *P < 0.05). Data are represented as means ± SEM.

Source data are available online for this figure.

allele, while the other allele with the missense TMD mutation is incapable of supporting normal hearing, as would have been expected for one wild-type allele (Yasunaga *et al*, 1999; Rodríguez-Ballesteros *et al*, 2008). Hence, we suspected that the TMD mutation impairs, but does not fully abolish, ER targeting of otoferlin and consequently, set out to study the insertion of opsin-tagged p.Ile1967del-otoferlin into microsomes *in vitro* (as performed above, Fig 2). Indeed, introducing the TMD mutation nearly halved the amount of glycosylated opsin-tagged otoferlin, which is consistent with drastically reduced ER targeting once the hydrophobic TMD recognized by TRC40 is shortened (Fig 8C).

In addition, psychophysical and electrophysiological measurements were collected from human subject E952-II:1 with the TMD mutation at the age of 2 years, when the child showed delayed language development. In line with data collected from computed tomography and MRI scans of the head, neither growth nor motor

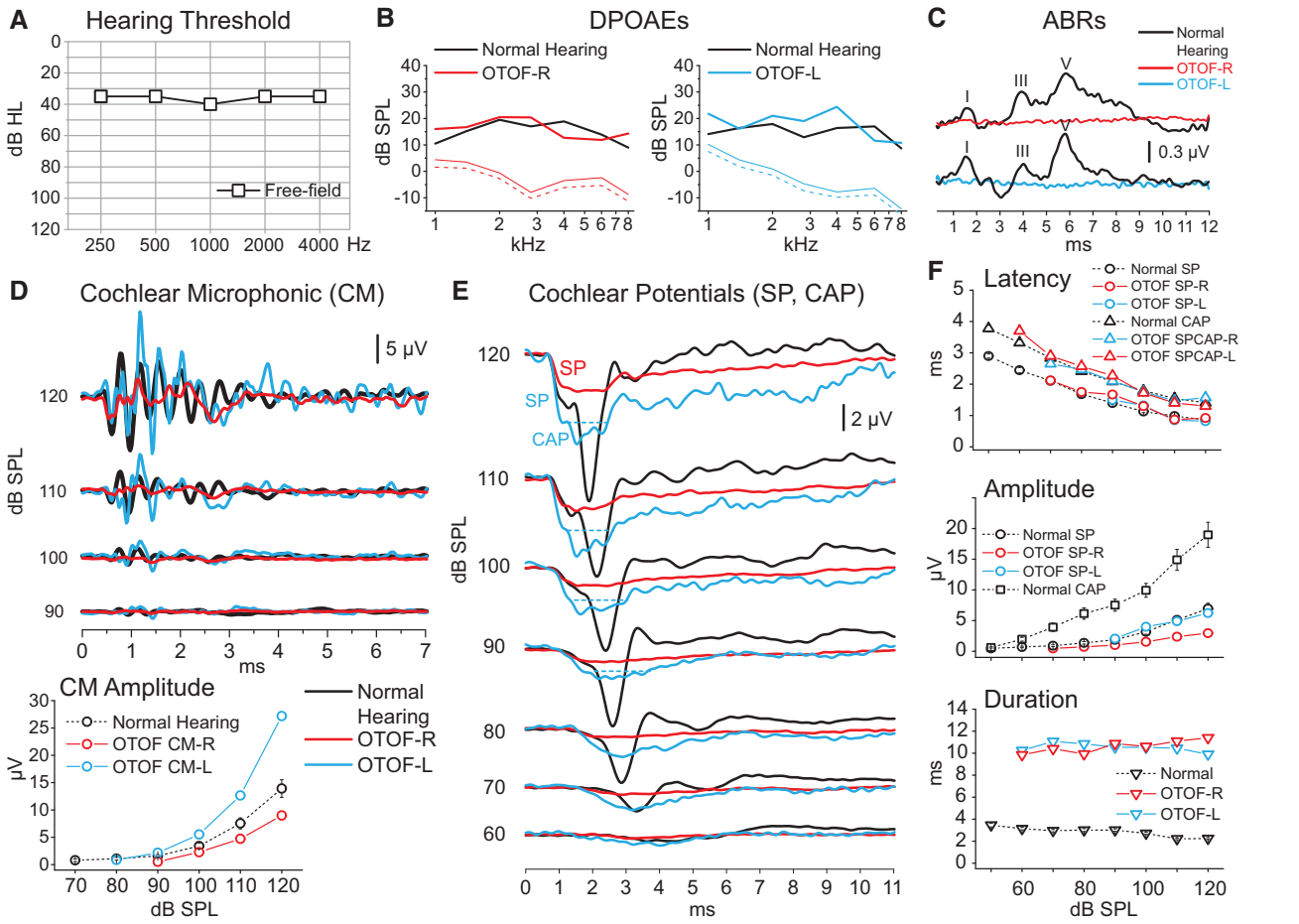

Figure 9. Auditory synaptopathy caused by transmembrane domain mutation in *OTOF*.

A Visual reinforcement audiometry performed in the free field: a mild hearing loss.

B, C Distortion product otoacoustic emissions (DPOAEs, B) were detected in each ear, whereas auditory brainstem responses (ABR, C) were lacking, together providing the signature of auditory synaptopathy or neuropathy.

D, E Cochlear microphonic potentials (CM), summating potential (SP), and compound action potential (CAP) recorded through transtympanic electrocochleography (ECochG) in response to clicks at decreasing stimulus intensities are superimposed on the corresponding potentials recorded from one normally hearing control. CM amplitudes were within normal limits (range as measured at 120 dB 4.31–28.02 µV in 20 normally hearing children). The ECochG waveform resulting from CM cancellation in the control begins with an abrupt negative deflection, the SP, followed by a negative peak, the neural CAP. In the child with the *OTOF* TMD mutation, the ECochG responses begin with a rapid negative deflection that peaks at the same latency as the SP in the control and has comparable amplitude. This is followed by a low-amplitude negative potential that peaks at the same CAP in controls but shows a markedly prolonged duration. In all graphs, time "0" refers to CM onset. R: right, L: left.

F Means and standard errors of peak latency and amplitude are reported for each potential category.

development showed any obvious abnormalities. In contrast to the profound deafness typically found in DFNB9 with inactivating mutations in both alleles of *OTOF* (Yasunaga *et al*, 1999; Rodríguez-Ballesteros *et al*, 2008), we found only a mild threshold increase in visual reinforcement audiometry performed in the free field (Fig 9A). We found maintained DPOAEs indicating intact OHC function (Fig 9B), but a lack of ABR (Fig 9C). Transtympanic electrocochleography (Fig 9D–F) revealed cochlear microphonic potentials (confirming intact OHC function) and summating potentials (reflecting the summed IHC receptor potential), but, importantly, failed to detect the SGN compound action potential. Taken together, the phenotype of the patient reflects a non-syndromic auditory synaptopathy (reviewed in Moser & Starr, 2016). In conclusion, we propose that the hearing impairment of *pwi* fish, $Wrb^{fl/fl}$:Cre^{A} mice, and the child with the TMD mutation is primarily caused by impaired ER targeting of otoferlin causing an auditory synaptopathy.

Discussion

This study demonstrates the requirement of the TRC40 pathway for efficient guided entry into the ER of the TA protein otoferlin in sensory HCs. Disruption of Wrb in zebrafish and mice dramatically reduced otoferlin levels in HCs and impaired sound encoding of the mouse cochlea, in a manner comparable to otoferlin missense

mutations that similarly decrease otoferlin levels. Hearing was partially restored upon transgenic Wrb rescue or otoferlin overexpression in the zebrafish *wrb* mutant *pwi*. A human mutation affecting the TMD of otoferlin not only resulted in auditory synaptopathy, but also impaired TRC40-dependent ER targeting of otoferlin *in vitro*. Therefore, we postulate that the impaired ER insertion of otoferlin is the main cause of the hearing impairment found in *Wrb* mutant fish and mice. We propose that the observed reduction in otoferlin levels limits the rate of vesicle replenishment at the hair cell synapse and thereby impairs sound encoding in *Wrb* mutants.

Studying the TRC40 pathway in sensory epithelia

Insertion of TA proteins via the recently discovered GET/TRC40 pathway is likely common to all eukaryotic cells. Insights into the molecular components of this pathway have been gained primarily in yeast and mammalian *in vitro* targeting systems as well as in cell lines. Here, we studied the presence, subcellular organization and function of this pathway in native tissues of fish and mice. Our choice of sensory epithelia was motivated by reports on sensory deficits upon genetic disruption of *wrb* in zebrafish (Gross *et al*, 2005; Lin *et al*, 2016) and *Caml* in mice (Bryda *et al*, 2012).

WRB was required for TRC40/ATP-dependent ER-insertion of the TA protein otoferlin, which could be inhibited by adding coiled-coil domains of WRB and CAML in an *in vitro* insertion assay. The efficiency of otoferlin insertion in this assay was lower than that of the previously studied TA protein Ramp4, as was the difference between membrane insertion with and without ATP (Favaloro *et al*, 2010). The reasons for these differences, as well as precise molecular mechanisms of ER-insertion of otoferlin in the absence of functional TRC40/WRB, remain to be investigated in future studies. Possible mechanisms include unassisted membrane targeting, as observed for cytochrome b5 (Brambillasca *et al*, 2006) or alternative pathways that employ chaperones of the Hsc70/Hsp40 families or the signal recognition particle (Rabu *et al*, 2008; Johnson, 2012). To date, the relative physiological relevance of the different pathways by which TA proteins can be targeted to the ER membrane has not been addressed. However, the drastic reduction in otoferlin levels in Wrb-deficient hair cells, as well as blocking insertion into ER microsomes *in vitro* by depletion of TRC40, indicates that efficient membrane insertion of otoferlin in hair cells critically requires the TRC40 pathway. Our otoferlin overexpression experiment indicates that, if forced, ER targeting of otoferlin by alternative pathways can partially restore auditory function in *pwi* zebrafish mutants. Future studies will also need to elucidate the fate of non-inserted TA proteins. In the case of otoferlin, our data suggest lysosomal protein degradation after translation, as global otoferlin levels were strongly reduced in Wrb-deficient IHCs, while we observed a concomitant increase in the occurrence of lysosomes throughout the IHC cytoplasm.

We note that this is the first study addressing ER targeting of TA proteins relevant for HC biology and that the reduced insertion of other TA proteins might additionally contribute to the observed hearing impairment. However, of the other synaptic TA proteins (https://shield.hms.harvard.edu/), neuronal synaptobrevins and syntaxins seem less likely to contribute to the synaptic phenotype, as IHCs appear to operate without these neuronal SNAREs (Nouvian *et al*, 2011). A recent study using *Math1-Cre*-mediated disruption of Caml in mouse reported a lack of HCs and deafness at 8 weeks of age and attributed this to a requirement of Caml for HC development (Bryda *et al*, 2012). Our study indicates initially normal development of HCs despite Wrb disruption. Stereocilia and HC synapses were formed normally, and we did not find a significant loss of IHCs up to 3 weeks of age, when hearing impairment is already prominent (see Figs 3 and EV5A′). Functionally, we found normal MET as well as voltage-gated Ca^{2+} currents in Wrb-deficient IHCs. These findings strongly argue that Wrb is not essential for HC development and several aspects of HC function. However, we did observe a progressive loss of IHCs that became obvious from > 4 weeks of age (Appendix Fig S4) and likely contributed to the absence of ABRs in > P29 $Wrb^{fl/fl}$:Cre^{A} animals (Fig 3A″ and B″). This observation is in line with the findings of Bryda and colleagues (Bryda *et al*, 2012) and highlights the importance of the TRC40 receptor comprised of Wrb and Caml in the ER targeting of TA proteins in IHCs.

Is partial otoferlin deficiency the key mechanism of the Wrb-related hearing impairment?

Considering (i) the concomitant impairment of HC otoferlin levels and hearing upon Wrb disruption and the partial restoration of hearing upon *wrb* rescue and otoferlin overexpression in *pwi* zebrafish mutants, (ii) the similar auditory phenotypes in *Wrb*- and otoferlin-deficient mice, and finally, (iii) the auditory synaptopathy in a human subject carrying an ER-targeting-deficient otoferlin, we postulate that the impaired ER-insertion of otoferlin is major mechanism contributing to the hearing impairment observed in *Wrb* mutant fish and mice. In the present study, we used the Vglut3-promoter to drive Cre expression in hair cells, which in the cochlea caused recombination in most if not all IHCs, but only in very few OHCs. Importantly, recombination was never observed in SGNs. Accordingly, cochlear amplification—mediated by OHCs—was intact, as shown by normal DPOAE, which also demonstrates normal cochlear function upstream of hair cell transduction (i.e. stria vascularis). Impaired neural responses to sound, despite intact cochlear amplification, signify auditory synaptopathy or neuropathy resulting from dysfunction or loss of IHCs, their afferent synapses and/or SGNs (recent review in (Moser & Starr, 2016). We attribute the hearing impairment to presynaptic dysfunction of IHCs, because mechanoelectrical transduction and the number of synapses with SGNs were normal in *Wrb*-deficient IHCs (Fig EV4). Specifically, we found that vesicle replenishment of active zones was impaired, while Ca^{2+} influx, Ca^{2+} influx–exocytosis coupling and vesicle fusion remained intact.

A concurrent reduction in otoferlin abundance and vesicle replenishment rate in IHCs, as well as absent ABRs, have previously been described for the *pachanga* mouse mutant (Pangrsic *et al*, 2010). There, the substitution of a single amino acid in the C_2F domain led to deafness, which we attributed—besides a potential functional impairment of otoferlin—to a reduction in otoferlin levels to 25% of wild type. Mice with IHC-specific Wrb disruption displayed an age-dependent reduction in IHC otoferlin levels, to roughly a third of wild-type levels by 3 weeks of age and the synchronized SGN activation by sound stimulation declined in parallel. It is tempting to speculate that the gradual decline of

otoferlin levels in Wrb-deficient IHCs reflects a progressive loss of the capacity of alternative ER-targeting mechanisms. The parallel reduction in otoferlin levels and synaptic sound coding supports a correlation of otoferlin levels, the rates of vesicle replenishment to the active zone, and SGN firing, as was recently proposed (Pangršič *et al*, 2012).

Finally, the finding of an auditory synaptopathy resulting from an *OTOF* mutation affecting the transmembrane domain (p.Ile1967del-otoferlin) and TRC40/ATP-dependent ER insertion supports the relevance of the TRC40 pathway for otoferlin biogenesis and hearing. As the frameshift mutation of the other *OTOF* allele is predicted to lead to nonsense-mediated decay, we assume that p.Ile1967del-otoferlin is the only available otoferlin variant. However, in contrast to previous findings, in which one functional *OTOF* allele suffices to enable normal hearing (Yasunaga *et al*, 1999; Rodríguez-Ballesteros *et al*, 2008), one allele coding p.Ile1967del-otoferlin proved insufficient. We speculate that p.Ile1967del-otoferlin, be it via impaired membrane insertion and consequently reduced abundance and/or function of p.Ile1967del-otoferlin in exocytosis, does not support the high rates of vesicle replenishment required for normal hearing. Here, our *in vitro* data seem to favor the membrane insertion scenario. A sufficient standing RRP, that is, the number of release sites occupied by release-ready vesicles, is required for faithful sound encoding, and its maintenance critically depends on vivid vesicle replenishment. When replenishment is impaired, the standing RRP strongly depends on the history of previous activity and, if too small, does not support temporally precise coding of sound onset and ongoing stimuli.

Materials and Methods

Animals

Animal handling was in accordance with national animal care guidelines, and all experiments were reviewed and approved by the animal welfare committees of the University of Göttingen and the State of Lower Saxony. The generation of $Wrb^{fl/fl}$ mice is described in the Appendix Supplementary Methods and Fig EV2, and that of transgenic *Vglut3-Cre* mice (Cre^{A}) in Jung *et al* (2015). The *Vglut3-ires-Cre* knock-in mice (Cre^{B}, used by the Boston group) were generated by L. Vong and B. Lowel (strategy and characterization unpublished) and first used in Lou *et al* (2013). A brief description of the construct and characterization is provided in the Appendix Supplementary Methods and Fig EV2. The generation of both reporter mouse lines has been described previously (Nakamura *et al*, 2006; Madisen *et al*, 2010). The generation of *wrb* (*pwi*) zebrafish has been described (Amsterdam *et al*, 2004). To conduct the acoustically induced startle reflex tests, individual 5-dpf wild-type or mutant larvae were stimulated in a 10-mm petri dish with a solid metal rod as in (Nicolson *et al*, 1998; Lin *et al*, 2016). All animal procedures performed at Harvard Medical School and UCSD were approved by Harvard Medical School and UCSD IACUC.

Human subjects

The propositus, subject E952-II:1, was diagnosed of isolated auditory neuropathy with no family history of hearing impairment and referred for genetic testing. After approval by the Ethical Committee of Hospital Universitario Ramón y Cajal (in accordance with the 1964 Declaration of Helsinki), written informed consent was obtained from all participants in the study (parents for themselves and for their son, who was minor).

Genetic study

DNA was extracted from peripheral blood samples by using the Chemagic MSM I automated system (Chemagen, Baesweiler, Germany). Screening for mutations in *OTOF*, the gene encoding otoferlin, was performed as previously reported (Rodríguez-Ballesteros *et al*, 2008). Mutation nomenclature is based on the cDNA sequence of the long cochlear *OTOF* isoform, which lacks exon 47 (GenBank accession number NM_001287489.1), and it follows current Human Genome Variation Society rules as implemented by the Mutalyzer 2.0.3 program (https://www.mutalyzer.nl/, Leiden University Medical Center, Leiden, the Netherlands).

Plasmids

For rescue of HCs of *pwi* fish, 2 µl (1×) or 4 µl (2×) of 25 ng/µl full-length zebrafish Wrb-EGFP or mouse otoferlin (mOtof) capped mRNA synthesized from a pCS2+ vector containing Wrb-EGFP or mOtof was injected into one-cell-stage embryos from crossing of *pwi* carriers. After behavioral testing, the larval genomic DNA was harvested and genotyped by PCR. To express zebrafish Wrb in hair cells, full-length Wrb or coiled-coil domain was PCR-amplified and inserted into Tol2 vectors containing EGFP and UAS-E1b sequence derived from the Tol2 kit (Kwan *et al*, 2007). To express ER-tdTomato, where tdTomato is flanked by zebrafish calreticulin 3a (GenBank: BC058314) at the N-terminus (amino acid 1–17) and an ER-targeting KDEL motif at the C-terminus, E1b-ER-tdTomato was inserted to the other side of the same UAS sequence driving Wrb-EGFP. Mosaic expression of transgenes in HCs was achieved by GAL4 driven by the hair cell promoter PPV3b (McDermott *et al*, 2010).

For pQET328-10hisZZ-OTOFop, the coding sequence of *Otof* (amino acids 1,733–1,997) was amplified from *pEGFP-Otof* using the following primer sequences: TATACAGGTACCGAGCTGCGGGTCA TCGTGTGGAACACAGACGAG and TAGTATAAGCTTTTAGCCCGTC TTGTTGGAGAAAGGCACGTAGAAGTTTGGGCCGGCCCCTAGGAGC TTCTT, containing *Kpn*I and *Hin*DIII restriction sites, respectively. This PCR reaction introduces a C-terminal opsin tag containing an *N*-glycosylation site. The fragment was cloned into pQET328-10hisZZtev (Favaloro *et al*, 2010). A *Nhe*I/*Avr*II fragment generated from pQET328-10hisZZ-OTOFop was cloned into pQE80-MBP-TRC40wt and pQE80-MBP-TRC40gr (Favaloro *et al*, 2010) to generate the constructs pT5L_T7-MBP-TRC40wt_hisZZ-OTOFop and pT5L_T7-MBP-TRC40gr_hisZZ-OTOFop, respectively, for bacterial expression of TRC40/OTOF complexes.

Protein purification and *in vitro* post-translational membrane insertion

Proteins were expressed in BL21-AI *E. coli* strain (see Appendix for details). The shortened form of otoferlin was used for better solubility. The TRC40gr mutant was described in Favaloro *et al* (2010).

Purification of HZZ-OTOFop and MBP-TRC40/HZZ-OTOFop complexes was performed essentially as described in Favaloro *et al* (2010). Purification of WRBcc and CAMLcyt was previously described in Vilardi *et al* (2011, 2014). Otoferlin membrane insertion assays were performed as described in Favaloro *et al* (2010). Where indicated, endoglycosidase H was used according to the manufacturer's instructions (New England Biolabs). WRBcc or CAMLcyt was added to the reaction as indicated in Fig 2C at 10 μM final concentration. Reaction mixtures were separated by SDS–PAGE and analyzed by immunoblot using a mouse monoclonal anti-opsin antibody (Adamus *et al*, 1991). We used ImageJ software (NIH, http://rsbweb.nih.gov/ij/) for densitometric analysis of the amount of glycosylated protein.

Immunohistochemistry and confocal microscopy of hair cells

For immunocytochemistry in zebrafish, 5-dpf larvae were fixed in 4% paraformaldehyde in PBS for 2 h at room temperature, cryoprotected by 30% sucrose, cryosectioned to 20 μm, and labeled with an anti-otoferlin antibody HCS-1 (Goodyear *et al*, 2010) overnight at 4°C. The sections were observed on an Olympus confocal FV1000 microscope with identical parameters (60×; 1.42 N.A. oil objective, laser intensity, photomultiplier gain, offset, and pixel dwell time). Images were later analyzed with ImageJ.

Murine cochlear explants were fixed in either (i) 4% formaldehyde in 120 mM sodium phosphate buffer for 1 h at 4°C or (ii) methanol for 20 min at −20°C and prepared as previously described (Khimich *et al*, 2005; Meyer *et al*, 2009). For quantitative analyses of organs of Corti from Wrb-deficient and control littermates, specimens were dissected, fixed, stained, and mounted, and IHCs from comparable tonotopic positions (~8 kHz region) imaged in parallel at all times. A minimum of three individual animals per genotype were processed in separate work streams; animal numbers and ages for each individual experiment are mentioned in the respective result sections, figure legends, or directly in the figure panels. The following primary antibodies were used: mouse anti-CtBP2 (Cat.-Nr. 612044; BD Biosciences), mouse anti-otoferlin (Cat.-Nr. ab53233, Abcam), rabbit anti-GluA2/3, mouse anti-GluR2 (Cat.-Nr. AB1506 and MAB397, both Merck Millipore), rabbit anti-VGlut3 (Cat.-Nr. 135 203; Synaptic Systems), and rat anti-LAMP1 (Cat.-Nr. MABC39, Millipore). Secondary AlexaFluor-568- and AlexaFluor-647-conjugated antibodies (Cat.-Nr. A11011, A11077, and A21236; Life Technologies) were applied for 1 h. Confocal image stacks were acquired with identical hardware and software settings, on either a Leica TCS SP2 or SP5 microscope (Leica Microsystems CMS) employing 10× air and/or 63× 1.4 NA oil immersion objectives and analyzed using custom MATLAB algorithms or ImageJ. For hair bundle stainings, Atto488-conjugated phalloidin (Cat.-Nr. 49409, Sigma Aldrich) was used; for nuclear stainings, 2-(4-amidinophenyl)-6-indolecarbamidine dihydrochloride (DAPI) was utilized (Cat.-Nr. D9542, Sigma Aldrich).

Auditory brainstem responses

Mice were anesthetized intraperitoneally with a ketamine (125 mg/kg)/xylazine (2.5 mg/kg) solution in 0.9% saline. Tone bursts (4–32 kHz, 10 ms plateau, 1 ms $\cos^2$ rise/fall) or clicks of 0.03 ms were generated using TDT System II hardware run by BioSig32 software (both Tucker-Davis Technologies) and presented at 40 Hz (tone bursts) or 20 Hz (clicks) in the free field ipsilaterally using a JBL 2402 speaker (JBL GmbH and Co.). The difference potential between subdermal needles placed on vertex and mastoid was amplified (50,000 times), filtered (low pass, 4 kHz; high pass, 400 Hz; Neuroamp amplifier), and averaged 1,300 times to obtain two mean ABRs for each sound intensity. ABR threshold was determined with 10 dB precision as the lowest stimulus intensity that evoked a reproducible response waveform in both traces by visual inspection.

Transmission electron microscopy

Electron microscopy of hair cell synapses was performed essentially as in (Wong *et al*, 2014). In brief, P19–24 mouse cochleas ($n_{animals}$ $Wrb^{+/+}$:Cre^{A} = 2; $Wrb^{fl/fl}$:Cre^{A} = 3) were dissected as described for immunohistochemistry and fixed for 1 h on ice with 4% paraformaldehyde and 0.5% glutaraldehyde in PBS (pH 7.2). Following additional fixation overnight on ice with 2% glutaraldehyde in 0.1 M sodium cacodylate buffer (pH 7.2), samples were washed in sodium cacodylate buffer and placed in 1% osmium tetroxide [(v/v) in 0.1 M cacodylate buffer] on ice for 1 h for further fixation. After a 1-h washing step in sodium cacodylate buffer and three brief washing steps in distilled water, samples were stained with 1% uranyl acetate (w/v in distilled water), dehydrated using an ethanol series, and then embedded in Epon resin. An Ultracut E microtome (Leica Microsystems, Wetzlar, Germany) equipped with a diamond knife (Diatome, Nidau, Switzerland) was used to obtain ultrathin sections (65–75 nm) of the specimen, which were then stained with 4% uranyl acetate (w/v in distilled water) and Reynold's lead citrate. Specimens were observed with a JEM 1011 transmission electron microscope (JEOL, Freising, Germany) and micrographs acquired by a Gatan Orius 1200A camera (Gatan GmbH, München, Germany) using the Digital Micrograph software package). Methods of EM-tomography are provided in the Appendix.

Patch-clamp recordings from IHCs

IHCs from acutely dissected apical coil organs of Corti (P14–P17) were used to record Ca^{2+} currents and exocytic membrane capacitance changes (ΔC_m) in the perforated patch configuration as previously described (Moser & Beutner, 2000). The pipette solution contained (in mM): 130 Cs-gluconate, 10 tetraethylammonium-Cl (TEA-Cl), 10 4-aminopyridine, 1 $MgCl_2 \cdot 6H_2O$, 10 Cs-HEPES, and 300 μg/ml amphotericin B (Calbiochem), pH 7.2. The extracellular solution contained (in mM) 110 NaCl, 2.8 KCl, 1 $MgCl_2 \cdot 6H_2O$, 35 TEA-Cl, 10 HEPES, 1 CsCl, 2 $CaCl_2$, and 2 mg/ml D-glucose, pH 7.3. EPC-9 amplifiers and Pulse/Patchmaster software (HEKA Elektronik) were used for all measurements. All voltages were corrected for liquid-junction potentials. Currents were low-pass filtered at 5 kHz and sampled at 10 kHz. Cells with holding currents exceeding −50 pA were discarded from the analysis. Ca^{2+} currents were further isolated using a P/n protocol. Series resistance was required to be below 30 MΩ; it averaged 22.4 ± 2.0 MΩ (in $Wrb^{fl/fl}$:Cre^{A}) and 24.4 ± 1.6 MΩ (in $Wrb^{+/+}$:Cre^{A}) at the beginning of the experiment and decreased thereafter.

Extracellular recordings from auditory nerve fibers

Single unit recordings from auditory nerve fibers of mice aged 20.4 ± 1.5 (means ± SEM) postnatal days ($Wrb^{fl/fl}$:Cre^{A}) and 22.5 ± 1.5 postnatal days ($Wrb^{+/+}$:Cre^{A}) days were performed as described (Taberner & Liberman, 2005; Jing *et al*, 2013). In brief, mice were anesthetized by i.p. injection of urethane (1.32 μg/g), xylazine (5 μg/g), and buprenorphine (0.1 μg/g), and parts of the occipital bone and cerebellum were removed to expose the anteroventral cochlear nucleus (AVCN). Sound-responsive single neurons were identified based on spontaneous and noise-induced action potential firing, and a basic characterization was performed by measuring their spontaneous rate, tuning curve, and post-stimulus time histograms. SGNs were discriminated from primary neurons of the AVCN by their discharge pattern, first spike latency, and stereotaxic position. Classification of neurons with low evoked spike rates (especially in Wrb-deficient animals) was difficult in some cases; however, errors would not be expected to have major impact on the results as response patterns of AVCN neurons showed the same alterations as SGNs (not shown). Recordings and offline analysis using waveform-based spike detection were performed using custom-written MATLAB software and TDT system III hardware and an ELC-03XS amplifier (NPI electronics).

Data analysis

Data analysis was performed using MATLAB (Mathworks), Igor Pro (Wavemetrics), and ImageJ (NIH) software. Immunofluorescence distributions, intensities, and cell shapes were measured using custom MATLAB routines. Means and grand averages are expressed as ± SEM. The Jarque–Bera and Kolmogorov–Smirnov tests for equal variances followed by two-tailed Student's *t*-test, or—when data were not normally distributed and/or variance was unequal between samples—the Mann–Whitney–Wilcoxon test were used for statistical comparisons between two samples. $*P < 0.05$, $**P < 0.01$, $***P < 0.001$.

Expanded View for this article is available online.

Acknowledgements
We thank N. Herrmann, S. Gerke, and C. Senger-Freitag for expert technical assistance. Moreover, we would like to extend our gratitude to Y. Li and B. Derfler for genotyping/maintaining the mouse colony; D.S. Zhang, P. Niksch, and B. Shrestha for tissue dissection; D. Scheffer for initial *Vglut3-ires-Cre* expression patterning; W. Fowle (Northeastern University) for the access to the SEM facility; and J Santini for microscopy facility (UCSD, supported by NIH NS047101). This work was supported by grants of the German Research Foundation through the Collaborative Research Center 889 (project A2 to T.M., A6 to N.S. and A7 to C.W.) and the Priority Program 1608 (to T.M. and N.S.), by the Center for Molecular Physiology of the Brain (FZT-103 to T.M.), and the Leibniz Program (to T.M.), by Deafness Research Foundation, and UCSD Foundation grants (to S-Y.L., S.M., and E.C.) by National Institutes of Health (NIH) grants R01-DC000304 and R01-DC002281 (to D.P.C.) and of the Instituto de Salud Carlos III, Madrid, Spain (FIS PI14/01162, Plan Estatal de I+D+I 2013–2016, with co-funding from the European Regional Development Fund, to I.C.). D.P.C. is an investigator of the Howard Hughes Medical Institute.

Author contributions
The study was designed by S-YL, DPC, TM, TP, CV, BS, NS, RS and IC. The experimental work was performed by CV (Ca^{2+} current and C_m recordings, immunohistochemistry, *Vglut3-Cre*^{A} expression study), IP (immunohistochemistry, PCR, Ca^{2+} current, and C_m recordings), GY and NS (*in vivo* extracellular recordings), CW (transmission electron microscopy [TEM]), SJM, EC, and S-YL (zebrafish work), S-YL (targeting vector design and mouse mutagenesis, FV (*in vitro* targeting assay), AAI (scanning electron microscopy [SEM], mechanotransduction current recordings, FM1-43 uptake, *Vglut3-Cre*^{B} expression study), TP (Ca^{2+} current and C_m recordings), XW (ABR recordings in *Vglut3-Cre*^{B} mice), SMW (*Vglut3-Cre*^{A} mice) and KYK (*Wrb* conditional KO mouse), MR-B and IC (human genetics), RS (audiology), TW (cloning of plasmids), and SJ (viral gene transfer). All authors prepared the manuscript.

Conflict of interest
The authors declare that they have no conflict of interest.

References

Adamus G, Zam ZS, Arendt A, Palczewski K, McDowell JH, Hargrave PA (1991) Anti-rhodopsin monoclonal antibodies of defined specificity: characterization and application. *Vision Res* 31: 17 – 31

Amsterdam A, Nissen RM, Sun Z, Swindell EC, Farrington S, Hopkins N (2004) Identification of 315 genes essential for early zebrafish development. *Proc Natl Acad Sci USA* 101: 12792 – 12797

Bozkurt G, Stjepanovic G, Vilardi F, Amlacher S, Wild K, Bange G, Favaloro V, Rippe K, Hurt E, Dobberstein B, Sinning I (2009) Structural insights into tail-anchored protein binding and membrane insertion by Get3. *Proc Natl Acad Sci USA* 106: 21131 – 21136

Brambillasca S, Yabal M, Makarow M, Borgese N (2006) Unassisted translocation of large polypeptide domains across phospholipid bilayers. *J Cell Biol* 175: 767 – 777

Bryda EC, Johnson NT, Ohlemiller KK, Besch-Williford CL, Moore E, Bram RJ (2012) Conditional deletion of calcium-modulating cyclophilin ligand causes deafness in mice. *Mamm Genome Off J Int Mamm Genome Soc* 23: 270 – 276

Cho S, Li G-L, von Gersdorff H (2011) Recovery from short-term depression and facilitation is ultrafast and Ca^{2+} dependent at auditory hair cell synapses. *J Neurosci* 31: 5682 – 5692

Denic V, Dötsch V, Sinning I (2013) Endoplasmic reticulum targeting and insertion of tail-anchored membrane proteins by the GET pathway. *Cold Spring Harb Perspect Biol* 5: a013334

Dulon D, Safieddine S, Jones SM, Petit C (2009) Otoferlin is critical for a highly sensitive and linear calcium-dependent exocytosis at vestibular hair cell ribbon synapses. *J Neurosci* 29: 10474 – 10487

El Mestikawy S, Wallén-Mackenzie A, Fortin GM, Descarries L, Trudeau L-E (2011) From glutamate co-release to vesicular synergy: vesicular glutamate transporters. *Nat Rev Neurosci* 12: 204 – 216

Favaloro V, Spasic M, Schwappach B, Dobberstein B (2008) Distinct targeting pathways for the membrane insertion of tail-anchored (TA) proteins. *J Cell Sci* 121: 1832 – 1840

Favaloro V, Vilardi F, Schlecht R, Mayer MP, Dobberstein B (2010) Asna1/TRC40-mediated membrane insertion of tail-anchored proteins. *J Cell Sci* 123: 1522 – 1530

Frank T, Rutherford MA, Strenzke N, Neef A, Pangršič T, Khimich D, Fejtova A, Gundelfinger ED, Liberman MC, Harke B, Bryan KE, Lee A, Egner A, Riedel D, Moser T (2010) Bassoon and the synaptic ribbon organize Ca^{2+}

channels and vesicles to add release sites and promote refilling. *Neuron* 68: 724 – 738

Furukawa T, Matsuura S (1978) Adaptive rundown of excitatory post-synaptic potentials at synapses between hair cells and eight nerve fibres in the goldfish. *J Physiol* 276: 193 – 209

Gale JE, Marcotti W, Kennedy HJ, Kros CJ, Richardson GP (2001) FM1-43 dye behaves as a permeant blocker of the hair-cell mechanotransducer channel. *J Neurosci Off J Soc Neurosci* 21: 7013 – 7025

Goodyear RJ, Legan PK, Christiansen JR, Xia B, Korchagina J, Gale JE, Warchol ME, Corwin JT, Richardson GP (2010) Identification of the hair cell soma-1 antigen, HCS-1, as otoferlin. *J Assoc Res Otolaryngol* 11: 573 – 586

Goutman JD, Glowatzki E (2007) Time course and calcium dependence of transmitter release at a single ribbon synapse. *Proc Natl Acad Sci USA* 104: 16341 – 16346

Goutman JD (2012) Transmitter release from cochlear hair cells is phase locked to cyclic stimuli of different intensities and frequencies. *J Neurosci* 32: 17025 – 17036

Gross JM, Perkins BD, Amsterdam A, Egana A, Darland T, Matsui JI, Sciascia S, Hopkins N, Dowling JE (2005) Identification of zebrafish insertional mutants with defects in visual system development and function. *Genetics* 170: 245 – 261

Harris DM, Dallos P (1979) Forward masking of auditory nerve fiber responses. *J Neurophysiol* 42: 1083 – 1107

Horn HF, Brownstein Z, Lenz DR, Shivatzki S, Dror AA, Dagan-Rosenfeld O, Friedman LM, Roux KJ, Kozlov S, Jeang K-T, Frydman M, Burke B, Stewart CL, Avraham KB (2013) The LINC complex is essential for hearing. *J Clin Invest* 123: 740 – 750

Jing Z, Rutherford MA, Takago H, Frank T, Fejtova A, Khimich D, Moser T, Strenzke N (2013) Disruption of the presynaptic cytomatrix protein bassoon degrades ribbon anchorage, multiquantal release, and sound encoding at the hair cell afferent synapse. *J Neurosci* 33: 4456 – 4467

Johnson JL (2012) Evolution and function of diverse Hsp90 homologs and cochaperone proteins. *Biochim Biophys Acta* 1823: 607 – 613

Jung S, Maritzen T, Wichmann C, Jing Z, Neef A, Revelo NH, Al-Moyed H, Meese S, Wojcik SM, Panou I, Bulut H, Schu P, Ficner R, Reisinger E, Rizzoli SO, Neef J, Strenzke N, Haucke V, Moser T (2015) Disruption of adaptor protein 2μ (AP-2μ) in cochlear hair cells impairs vesicle reloading of synaptic release sites and hearing. *EMBO J* 34: 2686 – 2702

Kalbfleisch T, Cambon A, Wattenberg BW (2007) A bioinformatics approach to identifying tail-anchored proteins in the human genome. *Traffic* 8: 1687 – 1694

Khimich D, Nouvian R, Pujol R, tom Dieck S, Egner A, Gundelfinger ED, Moser T (2005) Hair cell synaptic ribbons are essential for synchronous auditory signalling. *Nature* 434: 889 – 894

Kwan KM, Fujimoto E, Grabher C, Mangum BD, Hardy ME, Campbell DS, Parant JM, Yost HJ, Kanki JP, Chien C-B (2007) The Tol2kit: a multisite gateway-based construction kit for Tol2 transposon transgenesis constructs. *Dev Dyn Off Publ Am Assoc Anat* 236: 3088 – 3099

Lin S-Y, Vollrath MA, Mangosing S, Shen J, Cardenas E, Corey DP (2016) The zebrafish pinball wizard gene encodes WRB, a tail-anchored-protein receptor essential for inner-ear hair cells and retinal photoreceptors. *J Physiol* 594: 895 – 914

Lou S, Duan B, Vong L, Lowell BB, Ma Q (2013) Runx1 controls terminal morphology and mechanosensitivity of VGLUT3-expressing C-mechanoreceptors. *J Neurosci Off J Soc Neurosci* 33: 870 – 882

Madisen L, Zwingman TA, Sunkin SM, Oh SW, Zariwala HA, Gu H, Ng LL, Palmiter RD, Hawrylycz MJ, Jones AR, Lein ES, Zeng H (2010) A robust and high-throughput Cre reporting and characterization system for the whole mouse brain. *Nat Neurosci* 13: 133 – 140

Marlin S, Feldmann D, Nguyen Y, Rouillon I, Loundon N, Jonard L, Bonnet C, Couderc R, Garabedian EN, Petit C, Denoyelle F (2010) Temperature-sensitive auditory neuropathy associated with an otoferlin mutation: deafening fever!. *Biochem Biophys Res Commun* 394: 737 – 742

Mateja A, Szlachcic A, Downing ME, Dobosz M, Mariappan M, Hegde RS, Keenan RJ (2009) The structural basis of tail-anchored membrane protein recognition by Get3. *Nature* 461: 361 – 366

McDermott BM, Asai Y, Baucom JM, Jani SD, Castellanos Y, Gomez G, McClintock JM, Starr CJ, Hudspeth AJ (2010) Transgenic labeling of hair cells in the zebrafish acousticolateralis system. *Gene Expr Patterns* 10: 113 – 118

Meyer AC, Frank T, Khimich D, Hoch G, Riedel D, Chapochnikov NM, Yarin YM, Harke B, Hell SW, Egner A, Moser T (2009) Tuning of synapse number, structure and function in the cochlea. *Nat Neurosci* 12: 444 – 453

Meyers JR, MacDonald RB, Duggan A, Lenzi D, Standaert DG, Corwin JT, Corey DP (2003) Lighting up the senses: FM1-43 loading of sensory cells through nonselective ion channels. *J Neurosci Off J Soc Neurosci* 23: 4054 – 4065

Moser T, Beutner D (2000) Kinetics of exocytosis and endocytosis at the cochlear inner hair cell afferent synapse of the mouse. *Proc Natl Acad Sci USA* 97: 883 – 888

Moser T, Starr A (2016) Auditory neuropathy – neural and synaptic mechanisms. *Nat Rev Neurol* 12: 135 – 149

Mukhopadhyay R, Ho Y-S, Swiatek PJ, Rosen BP, Bhattacharjee H (2006) Targeted disruption of the mouse Asna1 gene results in embryonic lethality. *FEBS Lett* 580: 3889 – 3894

Nakamura T, Colbert MC, Robbins J (2006) Neural crest cells retain multipotential characteristics in the developing valves and label the cardiac conduction system. *Circ Res* 98: 1547 – 1554

Nicolson T, Rüsch A, Friedrich RW, Granato M, Ruppersberg JP, Nüsslein-Volhard C (1998) Genetic analysis of vertebrate sensory hair cell mechanosensation: the zebrafish circler mutants. *Neuron* 20: 271 – 283

Nouvian R, Neef J, Bulankina AV, Reisinger E, Pangršič T, Frank T, Sikorra S, Brose N, Binz T, Moser T (2011) Exocytosis at the hair cell ribbon synapse apparently operates without neuronal SNARE proteins. *Nat Neurosci* 14: 411 – 413

Obholzer N, Wolfson S, Trapani JG, Mo W, Nechiporuk A, Busch-Nentwich E, Seiler C, Sidi S, Söllner C, Duncan RN, Boehland A, Nicolson T (2008) Vesicular glutamate transporter 3 is required for synaptic transmission in zebrafish hair cells. *J Neurosci Off J Soc Neurosci* 28: 2110 – 2118

Pangrsic T, Lasarow L, Reuter K, Takago H, Schwander M, Riedel D, Frank T, Tarantino LM, Bailey JS, Strenzke N, Brose N, Müller U, Reisinger E, Moser T (2010) Hearing requires otoferlin-dependent efficient replenishment of synaptic vesicles in hair cells. *Nat Neurosci* 13: 869 – 876

Pangršič T, Reisinger E, Moser T (2012) Otoferlin: a multi-C2 domain protein essential for hearing. *Trends Neurosci* 35: 671 – 680

Pangršič T, Gabrielaitis M, Michanski S, Schwaller B, Wolf F, Strenzke N, Moser T (2015) EF-hand protein Ca^{2+} buffers regulate Ca^{2+} influx and exocytosis in sensory hair cells. *Proc Natl Acad Sci USA* 112: E1028 – E1037

Pfaff J, Monroy JR, Jamieson C, Rajanala K, Vilardi F, Schwappach B, Kehlenbach RH (2016) Emery-Dreifuss muscular dystrophy mutations impair TRC40-mediated targeting of emerin to the inner nuclear membrane. *J Cell Sci* 129: 502 – 516

Rabu C, Wipf P, Brodsky JL, High S (2008) A precursor-specific role for Hsp40/Hsc70 during tail-anchored protein integration at the endoplasmic reticulum. *J Biol Chem* 283: 27504 – 27513

Revelo NH, Kamin D, Truckenbrodt S, Wong AB, Reuter-Jessen K, Reisinger E, Moser T, Rizzoli SO (2014) A new probe for super-resolution imaging of membranes elucidates trafficking pathways. *J Cell Biol* 205: 591 – 606

Rodríguez-Ballesteros M, del Castillo FJ, Martín Y, Moreno-Pelayo MA, Morera C, Prieto F, Marco J, Morant A, Gallo-Terán J, Morales-Angulo C, Navas C, Trinidad G, Tapia MC, Moreno F, del Castillo I (2003) Auditory neuropathy in patients carrying mutations in the otoferlin gene (OTOF). *Hum Mutat* 22: 451 – 456

Rodríguez-Ballesteros M, Reynoso R, Olarte M, Villamar M, Morera C, Santarelli R, Arslan E, Medá C, Curet C, Völter C, Sainz-Quevedo M, Castorina P, Ambrosetti U, Berrettini S, Frei K, Tedín S, Smith J, Cruz Tapia M, Cavallé L, Gelvez N *et al* (2008) A multicenter study on the prevalence and spectrum of mutations in the otoferlin gene (OTOF) in subjects with nonsyndromic hearing impairment and auditory neuropathy. *Hum Mutat* 29: 823 – 831

Roux I, Safieddine S, Nouvian R, Grati M, Simmler M-C, Bahloul A, Perfettini I, Le Gall M, Rostaing P, Hamard G, Triller A, Avan P, Moser T, Petit C (2006) Otoferlin, defective in a human deafness form, is essential for exocytosis at the auditory ribbon synapse. *Cell* 127: 277 – 289

Ruel J, Emery S, Nouvian R, Bersot T, Amilhon B, Van Rybroek JM, Rebillard G, Lenoir M, Eybalin M, Delprat B, Sivakumaran TA, Giros B, El Mestikawy S, Moser T, Smith RJH, Lesperance MM, Puel J-L (2008) Impairment of SLC17A8 encoding vesicular glutamate transporter-3, VGLUT3, underlies nonsyndromic deafness DFNA25 and inner hair cell dysfunction in null mice. *Am J Hum Genet* 83: 278 – 292

Schroeder MR, Hall JL (1974) Model for mechanical to neural transduction in the auditory receptor. *J Acoust Soc Am* 55: 1055 – 1060

Schuldiner M, Collins SR, Thompson NJ, Denic V, Bhamidipati A, Punna T, Ihmels J, Andrews B, Boone C, Greenblatt JF, Weissman JS, Krogan NJ (2005) Exploration of the function and organization of the yeast early secretory pathway through an epistatic miniarray profile. *Cell* 123: 507 – 519

Schuldiner M, Metz J, Schmid V, Denic V, Rakwalska M, Schmitt HD, Schwappach B, Weissman JS (2008) The GET complex mediates insertion of tail-anchored proteins into the ER membrane. *Cell* 134: 634 – 645

Seal RP, Akil O, Yi E, Weber CM, Grant L, Yoo J, Clause A, Kandler K, Noebels JL, Glowatzki E, Lustig LR, Edwards RH (2008) Sensorineural deafness and seizures in mice lacking vesicular glutamate transporter 3. *Neuron* 57: 263 – 275

Simpson PJ, Schwappach B, Dohlman HG, Isaacson RL (2010) Structures of Get3, Get4, and Get5 provide new models for TA membrane protein targeting. *Structure* 18: 897 – 902

Spassova MA, Avissar M, Furman AC, Crumling MA, Saunders JC, Parsons TD (2004) Evidence that rapid vesicle replenishment of the synaptic ribbon mediates recovery from short-term adaptation at the hair cell afferent synapse. *J Assoc Res Otolaryngol* 5: 376 – 390

Stefanovic S, Hegde RS (2007) Identification of a targeting factor for posttranslational membrane protein insertion into the ER. *Cell* 128: 1147 – 1159

Suloway CJ, Chartron JW, Zaslaver M, Clemons WM (2009) Model for eukaryotic tail-anchored protein binding based on the structure of Get3. *Proc Natl Acad Sci USA* 106: 14849 – 14854

Taberner AM, Liberman MC (2005) Response properties of single auditory nerve fibers in the mouse. *J Neurophysiol* 93: 557 – 569

Varga R, Kelley PM, Keats BJ, Starr A, Leal SM, Cohn E, Kimberling WJ (2003) Non-syndromic recessive auditory neuropathy is the result of mutations in the otoferlin (OTOF) gene. *J Med Genet* 40: 45 – 50

Varga R, Avenarius MR, Kelley PM, Keats BJ, Berlin CI, Hood LJ, Morlet TG, Brashears SM, Starr A, Cohn ES, Smith RJH, Kimberling WJ (2006) OTOF mutations revealed by genetic analysis of hearing loss families including a potential temperature sensitive auditory neuropathy allele. *J Med Genet* 43: 576 – 581

Vilardi F, Lorenz H, Dobberstein B (2011) WRB is the receptor for TRC40/Asna1-mediated insertion of tail-anchored proteins into the ER membrane. *J Cell Sci* 124: 1301 – 1307

Vilardi F, Stephan M, Clancy A, Janshoff A, Schwappach B (2014) WRB and CAML are necessary and sufficient to mediate tail-anchored protein targeting to the ER membrane. *PLoS ONE* 9: e85033

Vogl C, Cooper BH, Neef J, Wojcik SM, Reim K, Reisinger E, Brose N, Rhee J-S, Moser T, Wichmann C (2015) Unconventional molecular regulation of synaptic vesicle replenishment in cochlear inner hair cells. *J Cell Sci* 128: 638 – 644

Wong AB, Rutherford MA, Gabrielaitis M, Pangrsic T, Göttfert F, Frank T, Michanski S, Hell S, Wolf F, Wichmann C, Moser T (2014) Developmental refinement of hair cell synapses tightens the coupling of Ca2 + influx to exocytosis. *EMBO J* 33: 247 – 264

Yamamoto Y, Sakisaka T (2012) Molecular machinery for insertion of tail-anchored membrane proteins into the endoplasmic reticulum membrane in mammalian cells. *Mol Cell* 48: 387 – 397

Yamamoto Y, Sakisaka T (2015) The emerging role of calcium-modulating cyclophilin ligand (CAML) in posttranslational insertion of tail-anchored proteins into the endoplasmic reticulum membrane. *J Biochem* 157: 419 – 429

Yasunaga S, Grati M, Cohen-Salmon M, El-Amraoui A, Mustapha M, Salem N, El-Zir E, Loiselet J, Petit C (1999) A mutation in OTOF, encoding otoferlin, a FER-1-like protein, causes DFNB9, a nonsyndromic form of deafness. *Nat Genet* 21: 363 – 369

